SANDIA REPORT

SAND2004-0967
Unlimited Release
Printed March 2004

A Finite Element Formulation for Modeling Dynamic Wetting on Flexible Substrates and in Deformable Porous Media

R. A. Cairncross and S. Madasu; Department of Chemical Engineering; Drexel University; Philadelphia, PA 19104

P. Randall Schunk; Multiphase Transport Processes Department; Sandia National Laboratories; PO Box 5800; Albuquerque, New Mexico 87185-0834

Prepared by
Sandia National Laboratories
Albuquerque, New Mexico 87185 and Livermore, California 94550

Sandia is a multiprogram laboratory operated by Sandia Corporation, a Lockheed Martin Company, for the United States Department of Energy's National Nuclear Security Administration under Contract DE-AC04-94AL85000.

Issued by Sandia National Laboratories, operated for the United States Department of Energy by Sandia Corporation.

Available to DOE and DOE contractors from
U.S. Department of Energy
Office of Scientific and Technical Information
P.O. Box 62
Oak Ridge, TN 37831

Telephone: (865)576-8401
Facsimile: (865)576-5728
E-Mail: reports@adonis.osti.gov
Online ordering: http://www.osti.gov/bridge

Available to the public from
U.S. Department of Commerce
National Technical Information Service
5285 Port Royal Rd
Springfield, VA 22161

Telephone: (800)553-6847
Facsimile: (703)605-6900
E-Mail: orders@ntis.fedworld.gov
Online order: http://www.ntis.gov/help/ordermethods.asp?loc=7-4-0#online

SAND2004-0967
Unlimited Release
Printed December 2004

A Finite Element Formulation for Modeling Dynamic Wetting on Flexible Substrates and in Deformable Porous Media

R. A. Cairncross and S. Madasu
Department of Chemical Engineering
Drexel University
Philadelphia, PA 19104

P. Randall Schunk
Multiphase Transport Processes Department
Sandia National Laboratories
P.O. Box 5800
Albuquerque, New Mexico 87185-0834

Abstract

This report summarizes research advances pursued with award funding issued by the DOE to Drexel University through the Presidential Early Career Award (PECASE) program. Professor Rich Cairncross was the recipient of this award in 1997. With it he pursued two related research topics under Sandia's guidance that address the outstanding issue of fluid-structural interactions of liquids with deformable solid materials, focusing mainly on the ubiquitous dynamic wetting problem.

The project focus in the first four years was aimed at deriving a predictive numerical modeling approach for the motion of the dynamic contact line on a deformable substrate. A formulation of physical model equations was derived in the context of the Galerkin finite element method in an arbitrary Lagrangian/Eulerian (ALE) frame of reference. The formulation was successfully integrated in Sandia's Goma finite element code and tested on several technologically important thin-film coating problems. The model equations, the finite-element implementation, and results from several applications are given in this report. In the last year of the five-year project the same physical concepts were extended towards the problem of capillary imbibition in deformable porous media. A synopsis of this preliminary modeling and experimental effort is also discussed.

Intentionally Left Blank

Contents

1. Model for dynamic wetting lines on flexible substrates 6
2. Wetting and penetration in deformable porous media 53
3. References 54
4. Distribution: 58

1. Model for dynamic wetting lines on flexible substrates

1.1 Introduction

The methods and approaches resulting from this research project are applicable to many Sandia manufacturing technologies, most notably pulsed laser welding and component encapsulation. These processes share many essential physical features with thin-film coating flow technology, the main subject application of this report. For more information on Sandia-related applications of this research please see the following internal report: *P. R. Schunk, 2000. "TALE: An Arbitrary Lagrangian-Eulerian Approach to Fluid-Structure Interaction Problems", Sandia Technical Report (SAND 2000-0807).*

Wetting [5,12,19] plays a significant role in determining the quality of products coated from liquid solutions. For example, defects such as air entrainment [25] or other instabilities such as ribbing [8] can be reduced by proper control of wetting phenomena. Conventional rigid solids are often replaced by flexible solids to obtain uniformity in coating and to delay onset of ribbing defects. Mathematical modeling of deformation of the flexible substrate and motion of the wetting line give rise to a free surface problem. In this paper, we apply the finite element method with Arbitrary Lagrangian Eulerian (ALE) mesh motion to solve problems of dynamic wetting on flexible substrates.

Several researchers [c.f. 20,32] have developed finite element formulations for solving dynamic wetting on *rigid* solids. Wetting on rigid solids involves a discontinuity arising at the contact line due to an incompatibility between boundary conditions applied on the free surface and solid surface. This incompatibility leads to the so-called "Kinematic paradox" or a double-valued velocity at the wetting line. The discontinuity arising at the wetting line gives rise to unbounded force, which would make coating impossible and hence, the singularity has to removed. Navier slip condition [10,17,23,34,36,39], which allows for local slip near the wetting line, is one of the most common models used to remove this discontinuity. Christodoulou and Scriven [10] used the Navier slip condition for wetting in slide coating and Silliman and Scriven [34] used the Navier slip condition for flow from a sharp edged slot. Kistler [20] used two nodal unknowns at the contact node with no penetration condition applied to one velocity unknown in the normal direction to the web and Navier slip condition applied to the other unknown in the tangential direction to the web. Schunk [32] used collapsible elements, where he collapsed three nodes at the contact node and the velocity becomes triple-valued. Schunk used the kinematic condition on one of the velocity unknowns, the impenetrability condition on the other two velocity unknowns in the normal direction to the web and Navier slip condition on the momentum residual of the velocity in the tangential direction of the web. Zhou and Sheng [39] used exponential variation of velocity over a slip length to allow for slip and Navier slip condition. In this paper the Navier slip condition, which is used in wide range of applications is used to relieve the singularity in the liquid domain.

Modeling wetting on *flexible* substrates has several additional challenges (1) fluid-structural interactions along the solid-liquid interface, (2) motion of contact line across

deformable solid surface, and (3) an elastic singularity at the contact line. Arbitrary Lagrangian Eulerian (ALE) method of mesh motion can handle the motion of contact node needed for wetting on flexible substrates. In Lagrangian method of mesh motion the grid follows a fluid/solid element, while in the Eulerian method of mesh motion the grid is fixed in space. The Lagrangian method usually breaks down for free surfaces, which undergo excessive deformation while the Eulerian method requires complicated fixed grid algorithms to track the moving boundary for solving the free surfaces with dynamic wetting lines. In order to take the advantage of the computationally easy Lagrangian method and minimal mesh distortions in fixed grid of Eulerian method, Arbitrary Lagrangian Eulerian (ALE) [1,28,35,38] method of mesh motion was developed where the grid/mesh moves independently of the underlying material reducing the mesh deformations. ALE method encompasses the features of both Lagrangian and Eulerian methods. ALE method was used extensively in the past to study complex moving boundary/free surface problems such as two and three dimensional free surface flows [35], incompressible unsteady viscous free surfaces [28], compression molding of viscoelastic polymers [1] and Hot forming process [38].

Several mesh motion techniques have been used for modeling free surface problems. Algebraic mesh motion is one of the earliest ALE mesh motion schemes, which requires interpolation functions for the mesh points. One of the common interpolation methods is the method of spines used by Christoudoulou and Scriven [10] to study slide coating. The method of spines breaks down when the free surface is highly curved as shown by Saito and Scriven [30]. They used a combination of Cartesian and polar coordinate parameterization for studying the flow in the downstream end of a slot coater. Elliptical mesh generation [8,33] was developed to handle irregular domains with free surfaces without losing the desired orthogonality in the mesh lines and mesh smoothness. Elliptical mesh generation determines the nodal positions by solving a system of elliptical partial differential equations mapping from the computational to physical domain. The disadvantage of this method is that it requires many input constants, which do not have any physical meaning. Hanumanthu [15] used a novel combination of elliptical and spine method of mesh generation to solve three-dimensional free surface coating flows. pseudo solid mesh motion developed by Sackinger et al. [29] treats the mesh to be a compressible, elastic solid and solves the Cauchy's equation of equilibrium to determine the nodal positions subjected to boundary conditions. An advantage of pseudo solid mesh motion is that it gives a physical insight of the mesh motion. Physical insight about deformation in elastic solids can be used to understand relation between input parameters and mesh deformation. This method was used for three-dimensional modeling of static and dynamic wetting on rigid solids [6-7], slot coating [29] and blade coating [9].

The test problem for modeling dynamic wetting on flexible substrate in this paper is flow in the upstream end of a slot coater. Slot coating has been modeled by several researchers [11,13,16, 31] with rigid substrates. Higgins and Scriven [16] determined the bounds on coating bead operability in slot coating with rigid substrate. They assumed the upstream and downstream free surfaces to be arcs of circles, the downstream meniscus to be pinned. They considered the cases of upstream meniscus to be free, pinned and the pressure drop under the feed slot to be negligible. Sartor [31] made first attempt in slot coating to solve the free surfaces with the radius of curvature varying on the free surface. He modeled the slot-coating problem for rigid substrate with Galerkin's finite element

method with upstream meniscus free but downstream meniscus pinned. Cohen [11] modeled two-layer slot coating by assuming rectilinear flow between the die lip and the rigid substrate, through which he predicted the position of the interlayer and the separation line. Gates [13] modeled the slot coating process for rigid substrate using Galerkin's finite element method by allowing the upstream and downstream menisci to be free to move and solved the free surface location without assuming it to be of constant radius of curvature. This paper models the upstream end of a slot coater with flexible substrate using Galerkin's finite element method with the meniscus pinned and radius of curvature of the free surfaces varying.

In this paper, the first section describes the physical theory of dynamic wetting on flexible substrates and the mesh motion scheme for upstream end of a slot coater. The second section describes the Galerkin finite element method and application of boundary conditions to the fluid momentum, solid momentum and mesh motion equations. The third section discusses the results, which include comparison between the performance between rigid and flexible solid.

1.2 Physical theory for wetting on deformable substrates

1.2.1 *Model Formulation*

In a conventional slot coater as shown in Figure 1, the coating liquid is forced through a feed slot and applied to a moving substrate. This coating method involves an upstream meniscus where the wetting of the substrate takes place and downstream meniscus where the liquid is carried away on the substrate. In this paper, the upstream end, which is a prototype flow for dynamic wetting is modeled.

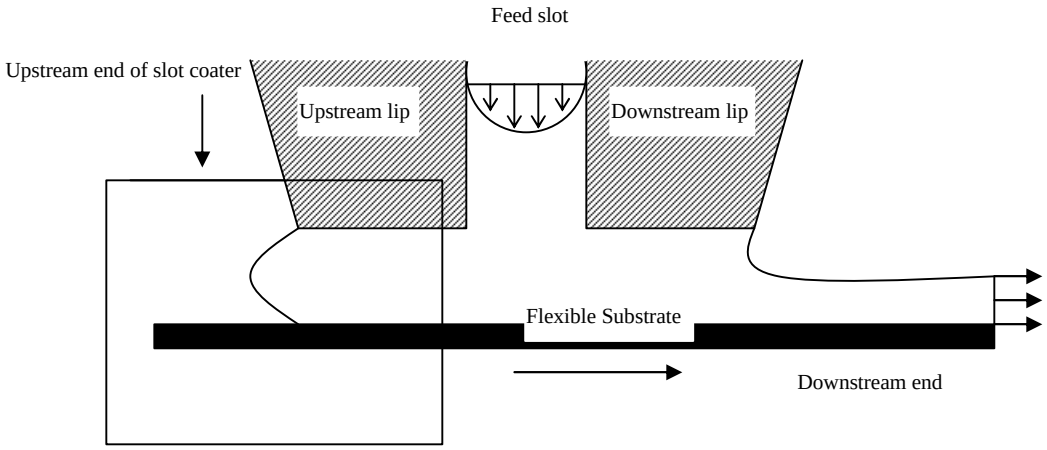

Figure 1. *Slot coater with uniform gap, upstream meniscus pinned to the upstream edge of the lip and flexible substrate used for coating.*

Wetting is influenced by substrate stiffness because deformation causes elastic forces that alter the force balances at the wetting line. Studying the effect of the substrate stiffness requires coupling the mechanics in the liquid and solid domains and conserving mass and momentum in both phases.

1.2.1.1 *Conservation of Mass and Momentum in Liquid Domain*

In the liquid phase, the momentum balance is given by Navier-Stokes equation and the mass balance is given by continuity equation. Coating flows are often laminar, steady state, two-dimensional and incompressible. Also, the gap is small enough that gravitational forces are negligible. At low Reynolds number the Navier-Stokes equation reduces to Stokes equation (1) in dimensionless form:

$$\nabla \bullet \mathbf{T_L} = 0 \qquad (1)$$

Where

$$\mathbf{T_L} = (-p_L \mathbf{I} + (\nabla \mathbf{v_L} + \nabla \mathbf{v_L}^T)) \qquad (2)$$

$\mathbf{T_L}$ is the stress tensor, p_L is the dimensionless pressure which is equal to $\frac{p'_L L}{m U_L}$, $\mathbf{v_L}$ is the velocity vector, L is the characteristic length scale, which is chosen to be the height of the liquid domain, U_L is the characteristic speed which is chosen to be as the speed of the undeformed solid, m is the viscosity of the liquid, p'_L is the dimensional pressure, and $\underline{\underline{\mathbf{I}}}$ is the identity tensor.

Conservation of mass for an incompressible fluid is given by the continuity equation:

$$\nabla \bullet \mathbf{v_L} = 0 \qquad (3)$$

1.2.1.2 *Reference Frame in Solid Domain*

The solid moving through the domain at *steady state* undergoes deformation. In our model we assume the velocity of the undeformed solid is uniform and that the solid is homogeneous and purely elastic. Based on these assumptions, the deformation at a fixed point in space is independent of time even though the solid is moving through the domain. The momentum and mass conservation equations can be written in either convecting Lagrangian frame or fixed Eulerian frame, in either of these reference frames the displacement is only a function of position if the solid is purely elastic.

In the Lagrangian frame of reference, $\mathbf{X_0}$ denotes the position of a material on the solid at time t=0 and at time t, $\mathbf{X}$ denotes the same material of the solid in a reference configuration which is undeformed and moving as a rigid solid. If $\mathbf{x}$ denotes the deformed coordinates in the Eulerian frame and **u** denotes the displacement which is a function of position then

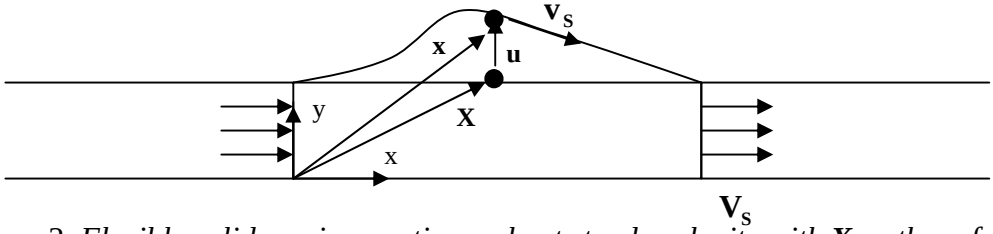

Figure 2. *Flexible solid moving continuously at steady velocity with **X** as the referential coordinates and **x** as the spatial coordinates.*

$$\mathbf{x} = \mathbf{X_o} + \mathbf{V_S}t + \mathbf{u} \tag{4}$$

$$\mathbf{x} = \mathbf{X} + \mathbf{u} \tag{5}$$

Where $\mathbf{X} = \mathbf{X_o} + \mathbf{V_S}t$, $\frac{d\mathbf{X}}{dt} = \mathbf{V_S}$ is the undeformed solid velocity in the reference configuration. In Lagrangian reference frame, **u** is a function of **X** only and in Eulerian reference frame it is a function of **x** only.

The mapping between the deformed coordinates at time t in the Eulerian reference frame and the undeformed coordinates in the reference configuration at the same time t is given by **x**=**x** (**X**). Oden and Lin [27] discussed the above shown referential coordinates for rotating deformable cylinder. In this paper, all the equations and boundary conditions both liquid and solid domains are in Eulerian frame of reference.

The velocity in the deformed coordinates can be decomposed to the velocity in the reference coordinates and a component due to deformation of the solid. The deformation gradient tensor transforms the velocity in the referential coordinates to the velocity in the deformed coordinates. The velocity of a particle changes with position, but the velocity at every position in space remains constant for all time at steady state.

$$v_{S,x} = \left(\frac{\partial x}{\partial t}\right)_{X_o} = \left(\frac{\partial x}{\partial X}\right)_t \left(\frac{\partial X}{\partial t}\right)_{X_o} + \left(\frac{\partial x}{\partial Y}\right)_t \left(\frac{\partial Y}{\partial t}\right)_{X_o} \tag{6}$$

$$v_{S,y} = \left(\frac{\partial y}{\partial t}\right)_{X_o} = \left(\frac{\partial y}{\partial X}\right)_t \left(\frac{\partial X}{\partial t}\right)_{X_o} + \left(\frac{\partial y}{\partial Y}\right)_t \left(\frac{\partial Y}{\partial t}\right)_{X_o} \tag{7}$$

Where $\left(\frac{\partial X}{\partial t}\right)_{X_o}, \left(\frac{\partial Y}{\partial t}\right)_{Y_o}$ are the rigid solid velocities in the referential coordinates.

$$\mathbf{v_S} = \mathbf{F} \bullet \mathbf{V_S} \tag{8}$$

Where $\mathbf{F} = \frac{\partial \mathbf{x}}{\partial \mathbf{X}}$ is the deformation gradient tensor, and $\mathbf{v_S}$ is the dimensionless solid velocity in the deformed coordinates.

1.2.1.3 *Conservation of Mass and Momentum in Solid Domain*

In the solid domain, the displacement field is described by Cauchy's equation of equilibrium along with the incompressibility condition. In our model, we assume that gravitational forces are negligible ($\mathrm{St_S} = \frac{\rho_S g L^3}{G u^2} = 0$) and that inertia is negligible ($\mathrm{Re_S} = \frac{\rho_S U^2 L^2}{G u^2} = 0$). This leads to Cauchy's equation of equilibrium in dimensionless form to equation (9). ρ_S is the density of the solid, g is the gravitational constant, U is the characteristic speed which is chosen to be as the speed of undeformed solid $V_{S,x}$, L is the characteristic length which is the height of the liquid domain, G is the shear modulus and u is the characteristic length scale for displacement which is chosen to be the height of the liquid domain.

$$\nabla \bullet \mathbf{T_S} = 0 \tag{9}$$

Where

$$\mathbf{T_S} = ((-p_s - 2 f G + G)\mathbf{I} + f\mathbf{B} - (1 - f)\mathbf{B}^{-1}) \tag{10}$$

Where the solid stress, $\mathbf{T_S}$, is predicted by the Mooney-Rivlin constitutive law [2] for incompressible, rubber-like solids, $p_s = \frac{p'_S L^2}{G u^2}$, p_S is the dimensionless pressure in the solid, p'_S is the dimensional pressure in the solid, f is a material constant which varies between 0 and 1, and $\mathbf{B} = \mathbf{F}\mathbf{F}^T$ is the left Cauchy-Green deformation tensor. $\mathbf{F}$ is the deformation gradient tensor in the deformed coordinates. The value of f does not significantly affect the vertical displacement in the parametric space used in this paper hence, f is chosen to be 1 [24]. The constant (-2 f G + G) $\mathbf{I}$ needs to be added to the constitutive law in order to make the solid stress go to zero when the displacement goes to zero.

Conservation of volume in the solid is given by incompressibility constraint, which requires the determinant of the deformation gradient tensor (represents the ratio of final volume to the initial volume) to be 1 as seen in equation (11).

$$|\mathbf{F}| = 1 \tag{11}$$

This concludes the equations that govern the velocity and pressure fields in liquid and displacement and pressure fields in the solid. The next section discusses the boundary conditions used on the upstream end of slot coater. The type of boundary conditions applied on the solid and liquid domains are indicated in Figure 3.

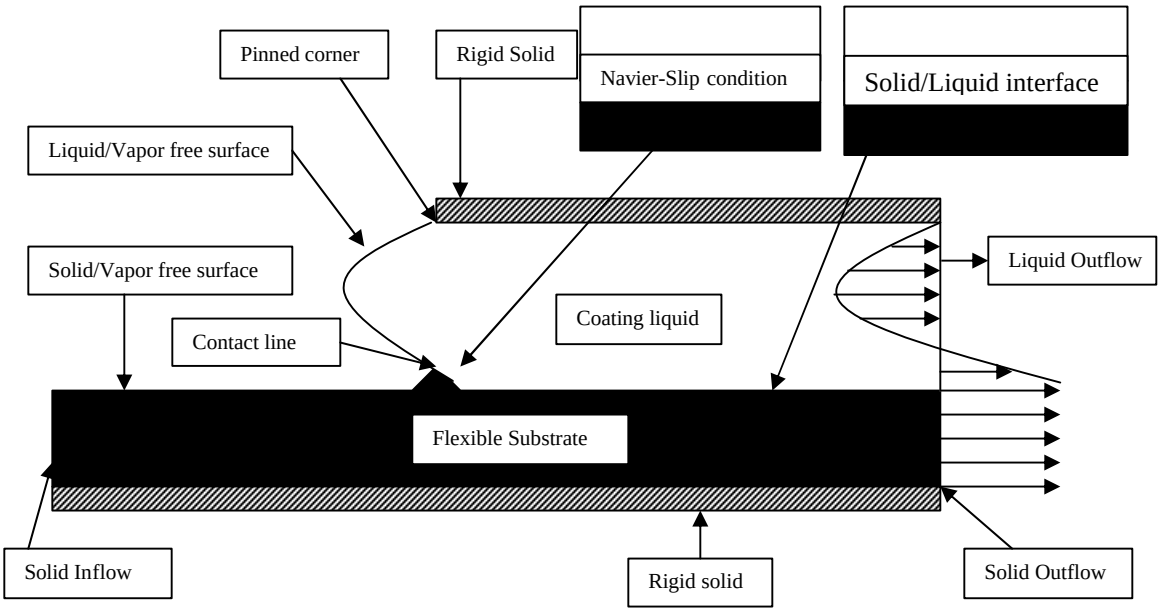

Figure 3. *Boundary conditions applied to the upstream end of Slot coater.*

1.2.2 *Boundary Conditions*

Boundary conditions are applied on the Navier-Stokes equation in the liquid domain and Cauchy's equation of equilibrium in the solid domain to solve for the velocity, pressure and displacement, pressure fields respectively.

1.2.2.1 *Boundary Conditions on Liquid Domain*

The flow in the liquid is primarily is shear flow between a stationary rigid solid at the upper surface and a moving substrate at the lower surface. The pressure gradient forces need to balance the Couette forces from the shear flow in the entire liquid domain for the net flow rate to be zero. At steady state, the liquid/vapor free surface is stationary but it changes its location such that net flow rate is zero.

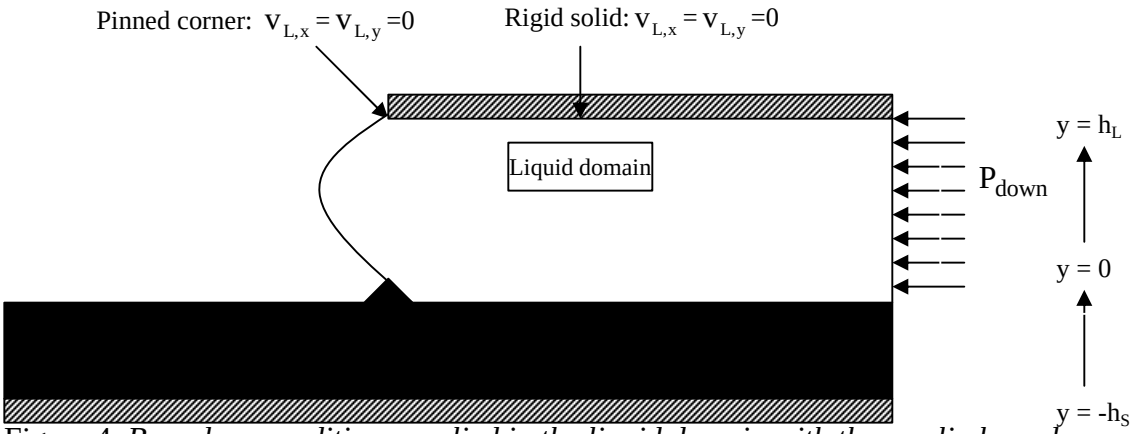

Figure 4. *Boundary conditions applied in the liquid domain with the no slip boundary condition applied at the rigid solid boundary.*

Along the liquid/vapor free surface, a normal stress balance condition is applied on the liquid velocity equations. This boundary condition balances the normal stress in the liquid, external pressure from the vapor and surface tension in the interface, and is normally called the *capillary boundary condition*:

$$-\vec{\mathbf{n}} \bullet \mathbf{T}_{\mathrm{L}} = \vec{\mathbf{n}} \bullet p_{\mathrm{ext}} \mathbf{I} + \frac{2 * \mathrm{H} * \vec{\mathbf{n}}}{\mathrm{Ca}} \qquad (12)$$

Where H is the surface mean curvature, Ca= $\frac{\mu V_{S,x}}{\sigma_{LV}}$ is the capillary number, σ_{LV} is the liquid/vapor surface tension. The capillary number scales the significance of the viscous forces to that of the surface tension forces at the liquid/vapor free surface.
At the liquid outflow plane, flow is assumed to be fully developed. There are two formulations for boundary conditions at the outflow: (1) Specify pressure at outflow and (2) Specify velocity profile.
Specifying pressure is one of the techniques for applying boundary conditions at the outflow. Pressure stresses are acting on the downstream end and hence the normal stresses are equated to the pressure and applied on the horizontal velocity with the vertical velocity being zero indicating no cross flow.

$$\vec{\mathbf{n}} \bullet \mathbf{T}_{\mathbf{L}} = -\vec{\mathbf{n}} \bullet P_{\mathrm{down}} \mathbf{I} \qquad (13a)$$

$$v_{L,y} = 0 \qquad (13b)$$

Alternate technique is to specify velocity profile. A fully developed flow boundary condition, which is Couette-Poiseuille flow, can be applied as a Dirichlet condition. The velocity profile for the fully developed flow with no net flow rate in dimensionless form is derived from the Navier-Stokes equation using the no slip boundary condition i.e. $v_{L,x} = V_{S,x}$ at y = 0 and $v_{L,x} = 0$ at y = h_L in dimensional form.

$$v_{L,x} = V_{S,x}\left[1 + 3\left(\frac{y}{h_L}\right)^2 - 4\left(\frac{y}{h_L}\right)\right] \qquad (14)$$

Where $V_{S,x}$ is the velocity of the liquid and is equal to the undeformed velocity of the solid, y is the dimensional position in the y-direction starting from the bottom of the solid domain.
The dirichlet condition of equation (14) can cause wiggles [14] at the outflow plane. Hence, specifying the pressure via equation (13) is used as the outflow boundary condition.

Along the solid/liquid interface, close to the wetting line, the singularity in stress in the liquid is relieved by using the *Navier slip condition,* which allows for local slip near the contact line. This slip transmits the momentum flux arising because of the discontinuity in the velocity of the liquid by the action of viscosity to the liquid. This condition is applied to the tangential component of the momentum equation at the interface.

$$\frac{1}{b}(\mathbf{v}_L - \mathbf{v}_S) = \vec{\mathbf{n}} \bullet \mathbf{T}_L \tag{15}$$

Where b is the slip coefficient. $b = 0$ corresponds to no slip condition whereas $b = \infty$ corresponds to free slip condition. The no penetration condition is applied to the normal component of the momentum equation, as the liquid does not penetrate the solid.

$$\vec{\mathbf{n}} \bullet \mathbf{v}_L = 0 \tag{16}$$

Away from the contact node (further than 2 elements) the no slip condition is applied and the velocity of the liquid is equal to velocity of solid. The velocity of the solid in the deformed coordinates is calculated from the velocity in the referential coordinates, which is uniform, and the deformation gradient tensor.

$$\mathbf{v}_L - \mathbf{v}_S = 0 \Rightarrow \mathbf{v}_L = \mathbf{F} \bullet \mathbf{V}_S \tag{17}$$

1.2.2.2 *Boundary Conditions on Solid Domain*

At the solid outflow, there is pressure force acting normal to the solid and shear force from the solid/liquid interface. Similar to the outflow boundary condition for the liquid (equation (14)), the solid displacement can be calculated as a fully developed profile using Cauchy's equation of equilibrium.

Cauchy's equation of equilibrium in two-dimensions with zero normal stress in y-direction and shear forces varying only in x-direction reduces to:

$$\frac{\partial \mathrm{T}_{s,xx}}{\partial \mathrm{x}} + \frac{\partial \mathrm{T}_{s,xy}}{\partial y} = 0 \tag{18}$$

Where $\mathrm{T}_{s,xx}$ is the stress in the x-direction and $\mathrm{T}_{s,xy}$ is the shear stress.

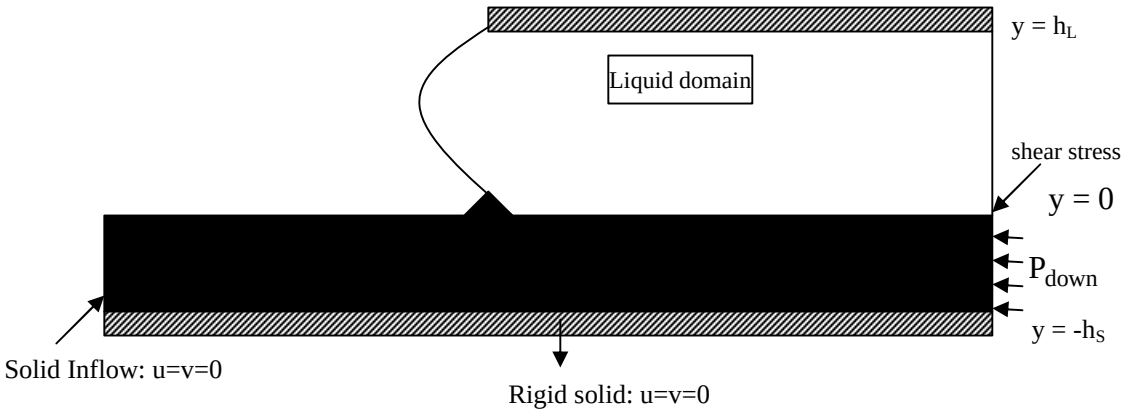

Figure 5. *Solid domain with the inflow boundary chosen far enough such that there is no displacement and no displacement boundary condition at the rigid solid.*

With $T_{s,xx} = -p$ and $T_{s,xy} = G\frac{du}{dy}$ and boundary conditions u = 0 at y = $-h_S$ and $T_{s,xy} = \frac{-4mV_{s,x}}{h_L}$ which can be derived from the Couette-Poiseuille flow velocity profile at y = 0

$$u = \left(\frac{3mV_{S,x}}{Gh_L^{\,2}}\right)y^2 - \left[\left(\frac{4mV_{S,x}}{Gh_L}\right)\right]y - \left(\frac{mV_{S,x}}{Gh_L}\right)h_S(3h_S + 4) \qquad (19)$$
$$= 3E_s\, y^2 - 4E_s y - E_S h_S(3h_S + 4)$$

u is the displacement in the x-direction, v is the displacement in the y-direction, h_S is the height of solid, h_L is the liquid film thickness, y is the dimensional position in the y-direction, G is the shear modulus and $E_s = \frac{mV_{s,x}}{G\,L} = \frac{\text{Viscous forces}}{\text{Elastic forces}}$. The Elasticity number scales the significance of the viscous forces along the solid/liquid interface to that of the elastic forces in the solid. An Elasticity number of zero corresponds to rigid solid and greater the elasticity number corresponds to a more flexible solid.
Along the solid/vapor free surface and solid/liquid interface, normal stress balance condition is used on the displacement of the solid. This boundary condition balances the normal stress in the solid, external pressure from the vapor or liquid and surface tension in the interface. Equation (20b) gives the normal stress from the liquid acting along the solid/liquid interface.

solid/vapor free surface

$$-\vec{\mathbf{n}} \bullet \mathbf{T}_S = \vec{\mathbf{n}} \bullet p_{ext}\mathbf{I} + \frac{2 * H * \vec{\mathbf{n}}}{Ca_{ESV}}; \qquad Ca_{ESV} = \frac{GL}{s_{SV}} \qquad (20a)$$

solid/liquid interface

$$-\vec{\mathbf{n}} \bullet \mathbf{T}_S = \vec{\mathbf{n}} \bullet \mathbf{T}_L * \mathrm{E}_S + \frac{2 * \mathrm{H} * \vec{\mathbf{n}}}{\mathrm{Ca}_{\mathrm{ESL}}}; \qquad \mathrm{Ca}_{\mathrm{ESL}} = \frac{\mathrm{GL}}{s_{\mathrm{SL}}} \tag{20b}$$

H is the surface mean curvature, $\mathrm{Ca}_{\mathrm{ESV}}$ is the elastic capillary number for solid/vapor free surface, $\mathrm{Ca}_{\mathrm{ESL}}$ is the elastic capillary number for solid/liquid interface, s_{SV} is the solid/vapor surface tension and s_{SL} is the solid/liquid surface tension. Elastic capillary number scales the elastic forces in the solid to the surface tension forces along the solid/vapor free surface or solid/liquid interface.

1.2.2.3 *Boundary Conditions at the Contact Line*

Mass and momentum balances in both the phases and geometric constraint in the form of contact angle determine the boundary conditions at the contact line. Conservation of mass in the liquid domain is obtained by applying the no penetration condition and the kinematic condition and in the solid domain by conforming the mesh to the solid.

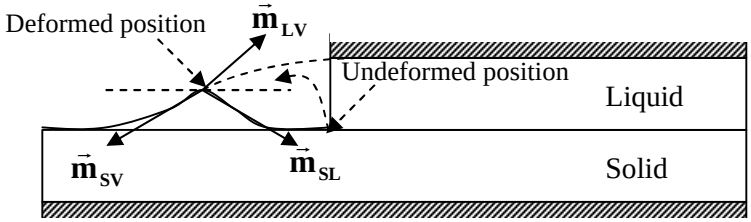

Figure 6. *Contact node motion under the influence of three surface tension forces, viscous forces and elastic forces.*

At the dynamic contact line, all the forces that enter the momentum equation need to be determined in order to implement the boundary conditions at the contact line. The first step requires modifying Young's equation [22] of force balance at the contact line. The forces acting in the vicinity of the contact line (as shown in Figure 7) are the three interfacial surface tensions arising at the contact line, elastic forces in the solid and viscous forces in the liquid:

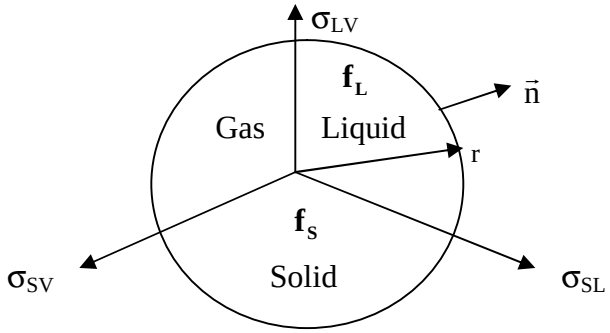

Figure 7. *Control volume for balancing forces in the vicinity of a dynamic contact line.*

$$\mathbf{f_s} + \mathbf{f_L} + \vec{\mathbf{m}}_{\mathbf{LV}} s_{\text{LV}} + \vec{\mathbf{m}}_{\mathbf{SV}} s_{\text{SV}} + \vec{\mathbf{m}}_{\mathbf{SL}} s_{\text{SL}} = 0 \quad (21)$$

$$\mathbf{f_S} = \lim_{\text{r}\to 0} \int_{q_{\text{SV}}}^{q_{SL}} \vec{\mathbf{n}} \bullet \mathbf{T_S}\ \text{r}\, dq\ ;\ \mathbf{f_L} = \lim_{r\to 0} \int_{q_{\text{SL}}}^{q_{\text{LV}}} \vec{\mathbf{n}} \bullet \mathbf{T_L}\ \text{r}\, dq \quad (22)$$

Where $\mathbf{f_s}$ is the force in the solid due to elastic stress, $\mathbf{f_L}$ is the force in the liquid due to stress in the liquid, $\vec{\mathbf{m}}_{\mathbf{LV}}$ is the tangent of the liquid/vapor free surface at the dynamic contact line, s_{LV} is the surface tension of the liquid/vapor free surface at the dynamic contact line, $\vec{\mathbf{m}}_{\mathbf{SV}}$ is the tangent of the solid/vapor free surface at the dynamic contact line, s_{SV} is the surface tension of the solid/vapor free surface at the dynamic contact line, $\vec{\mathbf{m}}_{\mathbf{SL}}$ is the tangent of the solid/vapor free surface at the dynamic contact line, s_{SL} is the surface tension of the solid/vapor free surface at the dynamic contact line, q_{SV} is the angular location of the solid/vapor free surface, q_{SL} is the angular location of the solid/liquid interface and q_{LV} is the angular location of the liquid/vapor free surface. Equation (21) is the force balance at the contact line and its application at the dynamic contact line is discussed in section 3.2.

The force $\mathbf{f_s}$ is finite but the elastic stress is singular. Singularity in elastic stress results at the contact line due to line force acting from the liquid/vapor surface tension. The line force acting at the contact line on an infinitesimal area results in an infinite displacement as given in [37]. But this is not observed physically as such a line force would rip the solid apart whereas a finite displacement actually results at the contact node. Hence, the line force should act on a finite contact region of molecular dimensions to give finite displacement. The solution for a distributed force over a finite contact region is given in [37]. The singularity in the solid is relieved by distributing the line force over a finite contact region.

Similarly, the force $\mathbf{f_L}$ is finite but stress is singular. A singularity in viscous stress results at the contact line due to the double-valued velocity. Huh and Scriven [18] developed a model for stress in the liquid for a rigid solid moving with a constant velocity and the liquid/vapor free surface making a finite angle with the solid. They assumed creeping flow in the liquid and rigid solid. A singularity in the liquid is arises due to the double valued velocity and leads to infinite stresses and non-physical results. But in reality, the stresses in the liquid are finite and hence the double valued velocity is relieved using Navier-slip condition.

Momentum balance requires all the three surface tensions and the forces arising at the contact node due to the stresses in the liquid and solid to be balanced. At the contact line it is desired that contact line moves along with the liquid/vapor free surface, and conforms to the solid domain with a contact angle θ at the contact line. The contact angle is a geometric constraint that is applied at the contact node by specifying the contact angle with respect to the bisecting plane. Mass is balanced in the solid at the contact node

by making the mesh to conform to the solid and not allowing for mass flux to leave the solid. This leads to setting the y-mesh displacement equal to the y-solid displacement. Based on the mass, momentum balances and geometric constraint, following set of boundary conditions are applied at the contact line:

- x - component of fluid momentum residual is replaced by kinematic condition -
- $v_{L,x} = 0$
- y - component of fluid momentum residual is replaced by no penetration - $v_{L,y} = 0$
- x - component of solid momentum residual is added to capillary condition from solid/liquid interface, solid/vapor and liquid/vapor free surfaces and normal stress from the liquid
- y - component of solid momentum residual is added to capillary condition from solid/liquid interface, solid/vapor and liquid/vapor free surfaces and normal stress from the liquid
- x - component of mesh displacement is replaced by contact angle condition with respect to the bisecting plane - $\vec{\mathbf{m}}_{\mathbf{LV}} \bullet \frac{(\vec{\mathbf{m}}_{\mathbf{SL}} - \vec{\mathbf{m}}_{\mathbf{SV}})}{|\vec{\mathbf{m}}_{\mathbf{SL}} - \vec{\mathbf{m}}_{\mathbf{SV}}|} = \cos ?$.
- y - component of mesh displacement is replaced by - dy = v (Contact node moves along with the real solid in the vertical direction)

1.2.3 *Mesh Motion Schemes*

The challenging aspect of the problem is that the mesh in the solid needs to conform to the solid and to be able to move with the liquid/vapor free surface. This aspect of the motion can be handled using an ALE method of mesh motion. We have tested two ALE mesh motion schemes for dynamic wetting: pseudo solid mesh motion [6,7,29] and an alternative mesh motion scheme based on spine method of mesh motion [10,15,30]. In the liquid domain, pseudo solid mesh motion is implemented and in the solid domain both pseudo solid and spine methods of mesh motion are tested.

1.2.3.1 *Pseudo Solid Mesh Motion*

Pseudo solid mesh motion moves the nodes as though they behave as an elastic solid by solving Cauchy's equation of equilibrium and the boundary conditions describing the physics of the problem.

If **X** denotes the position of a point in the initial configuration, **x** denotes the position in the final configuration and **d** denotes the displacement field that maps the initial domain to the final domain then

$$\mathbf{x} = \mathbf{X} + \mathbf{d} \qquad (23)$$

d is obtained by solving the field equations, boundary conditions on the mesh domain. For the mesh motion, we use Cauchy's equation of equilibrium with the assumptions of no body forces:

$$\nabla \bullet \mathbf{S} = 0 \qquad (24)$$

Where $\mathbf{S} = -l e \mathbf{I} + m * \mathbf{B}$. l, m are the Lame coefficients. e is the volume dilatation, which under small strain reduces to $\mathrm{tr}|\nabla \mathbf{d}|$.

Pseudo solid mesh motion [6,7,29] moves the nodes in the interior as an elastic solid so as to satisfy the applied boundary conditions. These boundary conditions are chosen such that they describe the physics of the problem. The mesh conforms to the boundaries when it deforms and hence, the final deformed shape of the mesh is the actual shape of the physical domain. Some of the boundary conditions that are applied on the mesh are shown in Figure 8.

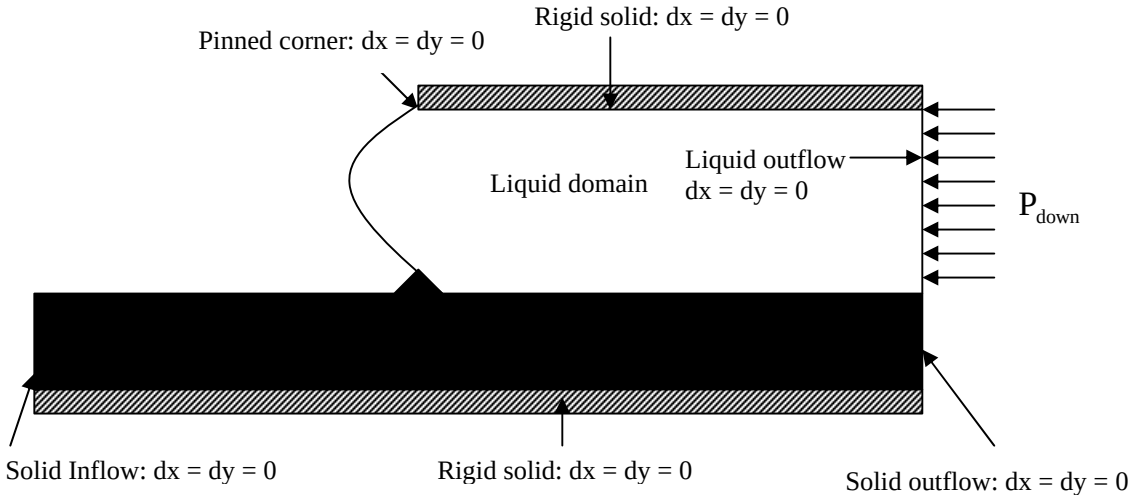

Figure 8. *Liquid domain with the zero displacement boundary condition applied at the rigid solid boundary, zero displacement applied at the pinned corner and zero displacement applied at the liquid outflow plane. dx is the x-displacement of the mesh and dy is the y-displacement of the mesh.*

Along the *liquid/vapor free surface*, a kinematic condition is applied on the displacement in the normal direction (x-displacement). The kinematic condition physically does not allow any normal velocity through the interface.

$$\vec{\mathbf{n}} \bullet \mathbf{v}_L = 0 \qquad (25)$$

Along the tangential direction (y-displacement), the nodes are allowed to be shear free so that they can freely slide and minimize element distortions.
Along the *solid/vapor free surface* and *solid/liquid interface*, the vertical motion of the mesh must conform to the solid. Hence the y-displacement of the mesh is set equal to the y-displacement of the solid:

$$dy = v \qquad (26)$$

For the x-displacement, the nodes are allowed to be shear free so that the nodes slide freely and their motion will become independent of the underlying solid. Tangential motion of the dynamic contact line along the solid surface will dictate motion of the node

associated with the contact line, and all other nodes on the solid surface will distribute to reduce shear of the mesh. The shear free boundary condition reduces element distortions.

1.2.3.2 *Spine Method of Mesh Motion*

When the dynamic contact line moves significantly upstream or downstream, pseudo solid mesh motion in the solid domain can lead to excessive mesh distortion near the contact line. An alternative mesh motion scheme based on spines and algebraic mesh generation results in less distortion. In this mesh motion scheme, the nodes are moved by using a stretching parameter, which is equal to the ratio of adjacent elements. Elements are stretched to be smaller closer to the dynamic contact line using the stretching parameters. Nodes align vertically along spines. Vertical distribution comes from setting the displacements of the nodes to be equal to the displacements of the solid:

$$v_{mesh} = v_{solid} \tag{27}$$

Where v_{mesh} is the displacement of the mesh and v_{solid} is the displacement of the solid. The spine method has the advantages of easy implementation and smaller memory usage. The elements are more concentrated near the contact node by stretching the elements more towards the contact node. The stretching function used is given in the equation (28)

$$\Delta x_1 = (L_{TOTAL} - L_{CR})\left(\frac{1-h}{1-h^{ne-1}}\right) \tag{28}$$

Where Δx_1 is the size of the first element adjacent to the element whose size is fixed, L_{TOTAL} is the total length of the domain over which stretching is applied and ne is the number of elements in the domain and h is the stretching parameter. $h > 1$ if the elements sizes are desired to increase over the domain and $h < 1$ if the elements sizes are desired to decrease over the domain.

1.3 GALERKIN FINITE ELEMENT FORMULATION

1.3.1 *Residual Calculations in the Finite Element Method*

Coating problems usually involve a free surface, which makes the boundary conditions nonlinear, and hence, numerical methods like the Finite Element method (FEM) are used. Galerkin's method with finite element basis functions method approximates the solution in each element to be the product of the nodal unknowns and the basis functions. The two-phase problem in this paper requires solving for the displacement, pressure and mesh displacement in the solid, and velocity, pressure, mesh displacement in the liquid. The basis functions for velocity and displacement unknowns are chosen to be biquadratic and for the pressure unknowns to be bilinear. The order of basis functions for pressure is chosen to be one order less than that of velocity or displacement in order to satisfy the Ladyzhenskaya-Babuska-Brezzi (LBB) condition [26].

The displacements fields in the solid domain is given by

$$u = \sum_{i=1}^{n} u_i f_i(x,y)\,;\; v = \sum_{i=1}^{n} v_i f_i(x,y) \tag{29}$$

The pressure field in the solid domain is given by

$$p_S = \sum_{i=1}^{m} p_{Si} y_i(x,y) \tag{30}$$

Where u is the solid displacement in x-direction, v is the solid displacement in the y-direction, p_S is the pressure in the solid domain, $f_i(x,y)$ denotes the biquadratic basis function, $y_i(x,y)$ is the bilinear basis function, n is the number of nodes in an element where the variable u or v are calculated which is 9 and m is the number of nodes in an element where the variable p_S is calculated which is 4.

The velocity fields in the liquid domain is given by

$$v_{L,x} = \sum_{i=1}^{n} v_{L,x_i} f_i(x,y)\,;\; v_{L,y} = \sum_{i=1}^{n} v_{L,y_i} f_i(x,y) \tag{31}$$

The pressure field in the liquid domain is given by

$$p_L = \sum_{i=1}^{m} p_{Li} y_i(x,y) \tag{32}$$

Where $v_{L,x}$ is the velocity of liquid in the x-direction, $v_{L,y}$ is the velocity of liquid in the y-direction, p_L is the pressure in the liquid domain.

The momentum residual in the liquid domain is integrated by parts using the basis function as weighting function. The weighted residual in the weak form is expressed as follows:

$$R_i^m = \int_V (\nabla \bullet \mathbf{T_L}) f_i \, dv = -\int_V (\nabla f_i \bullet \mathbf{T_L}) \, dv + \int_S f_i (\vec{\mathbf{n}} \bullet \mathbf{T_L}) \, ds \tag{33}$$

The Continuity residual is obtained as follows:

$$R_i^c = \int_V (\nabla \bullet \mathbf{v_L}) f_i \, dv \tag{34}$$

The momentum residual in the solid domain is obtained as follows:

$$R_i^m = \int_V (\nabla \bullet \mathbf{T_S}) f_i \, dv = -\int_V (\nabla f_i \bullet \mathbf{T_S}) \, dv + \int_S f_i (\vec{\mathbf{n}} \bullet \mathbf{T_S}) \, ds \tag{35}$$

The incompressibility residual in deformed co-ordinates is obtained as follows:

$$R_i^c = \int_V (\left|\underline{\underline{\mathbf{I}}} - \nabla \mathbf{u}\right| - 1) y_i \, dv \tag{36}$$

The second term in the momentum residual is a boundary condition term. For the capillary condition, the boundary integral term can be expressed in terms of surface divergence [6] and can be added to the residual. The details of this derivation are provided in [6].

1.3.2 *Momentum Balance at the Contact Node*

The total momentum that enters the residual equation at the contact node is obtained by adding the residual contributions from the solid and liquid domains:

$$\iint_V \nabla \bullet \mathbf{T} f_{DCL} \, dv = \iint_{V_S} \nabla \bullet \mathbf{T_S} f_{DCL} \, dv + \iint_{V_L} \nabla \bullet \mathbf{T_L} f_{DCL} \, dv \tag{37}$$

Where f_{DCL} is the weighting function that corresponds to the node at the dynamic contact line. Using the same approach of [24], equation (37) can be expressed by integrating by parts as shown in equation (33) to obtain contributions from all the surfaces and use the surface divergence theorem to express in terms of surface tension.

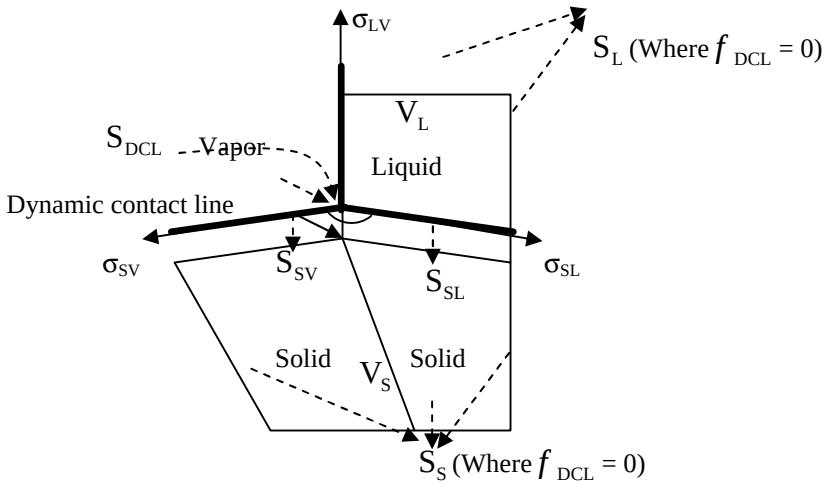

Figure 9. *Control volume over which momentum balance is written in the vicinity of the dynamic contact line. Bold lines indicate the interfaces. Quadrilaterals correspond to elements in mesh.*

$$\iint_V \nabla \bullet \mathbf{T} f_{DcL}\,dv = \mathbf{f_s} + \mathbf{f_L} + \vec{\mathbf{m}}_{\mathbf{LV}} s_{LV} + \vec{\mathbf{m}}_{SV} s_{SV} + \vec{\mathbf{m}}_{\mathbf{SL}} s_{SL} - \iint_{V_S} \mathbf{T_S} \bullet \nabla f_{DCL}\,dv$$
$$- \iint_{V_L} \mathbf{T_L} \bullet \nabla f_{DCL}\,d + \int_{S_{SL}} s_L \nabla_s f_{DCL}\,ds + \int_{S_{LV}} s_V \nabla_s f_{DCL}\,ds \qquad (38)$$
$$+ \int_{S_{SV}} s_{SV} \nabla_s f_{DCL}\,ds$$

Where ∇_s is the surface gradient operator [24]. The first five terms in the above residual disappear as a result of force balance obtained by the force balance at the dynamic contact line (equation (21)) shown in section 2.2.3 and hence the rest of the terms enter the momentum equation of the solid at the contact node.

1.3.3 *Application of Boundary Conditions*

In a two-dimensional model, the momentum equation results in two components along the two directions. The continuity equation is scalar equation and it serves as a constraint to determine pressure. The boundary conditions to the momentum equations are applied either by adding the stress (second term) resulted in equation (33) to the momentum equation (weak form) or by replacing the momentum equation and by a boundary condition such as a Dirichlet condition (strong form).

The Capillary boundary condition along the liquid/vapor free surface, solid/vapor free surface, solid/liquid interface; Navier slip condition close to the dynamic contact line; and liquid outflow boundary condition are applied in the weak form. Solid inflow, solid outflow, rigid solid, no slip condition, Lagrangian boundary condition on the mesh displacement, and pinned condition are applied as dirichlet conditions. The Contact angle condition and kinematic condition are applied in the strong form by wiping the entire residual and replacing it with the boundary condition.

3.4 *Method of Solving the Nonlinear Residual Equations*

The discretized residual equations resulting from applying the Galerkin finite element method are a system of nonlinear equations for the nodal values of field variables. These equations are linearized using the Newton's method [10,29] and the resulting matrix is solved for updates of the variables using a sparse solver [21], which performs LU decomposition and solves the matrix problem. Numerical integration is performed by gaussian quadrature over each element in two directions using four gauss points in each direction.

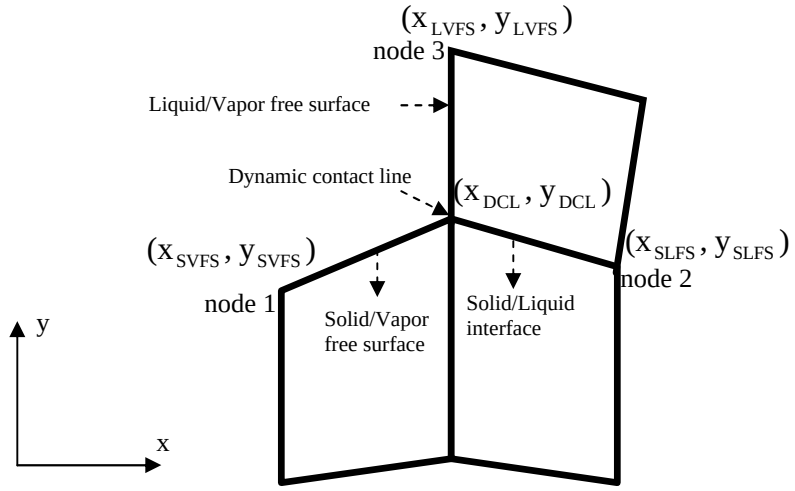

Figure 10. *Quadrilaterals correspond to elements in mesh. Constant element sizes in x-direction along the solid/vapor free surface and solid/liquid interface and in y-direction along the liquid/vapor free surface around the dynamic contact line.*

An additional constraint is placed on the deformed element sizes adjacent to the dynamic contact line such that they are constant in x-direction along the solid surface and in y-direction along the liquid/vapor free surface as shown in Figure 10.

$$x_{DCL} - x_{SVFS} = x_{SLFS} - x_{DCL} = y_{LVFS} - y_{DCL} = L_{CR} \qquad (39)$$

Where L_{CR} is the constant length of the element size adjacent to the contact node.

This constraint distributes the line force from the liquid/vapor free surface over an effective constant contact region. Equation (39) is applied as a Dirichlet condition on the x-mesh residuals at node 1 and node 2 and y-mesh residual at node 3. If this constraint is not applied, the trends of variation of dynamic contact line position with elasticity number changes depending upon the variation of the element sizes adjacent to the contact node.

Figure 11 shows the trends of the variation of dynamic contact line with elasticity number for spine and pseudo solid mesh motion schemes under the constraint of element size fixed and unfixed. The trends from the spine method and pseudo solid method match when the element size is fixed. When the element sizes are not fixed for the spine method, initially the dynamic contact line moves upstream with increase in elasticity number and then downstream but with the pseudo solid method the dynamic contact line always moves downstream with increase in elasticity number. Hence, in order for predictions for both mesh motion schemes to be consistent the elements adjacent to the contact node should be fixed. With the variation of elasticity number, depending upon whether the contact line moves upstream or downstream, the size of the elements

adjacent increase or decrease for the mesh motion schemes if they are not fixed. Hence, the stress acting at the contact line changes and causes the inconsistency.

1.4 TESTS OF MESH PERFORMANCE

1.4.1 *Mesh Convergence*

The first step in this analysis is to show that the numerical solutions presented are accurate solutions of the system of partial differential equations presented above. Here, convergence means with further refinement the change in the shapes of the solid and liquid/vapor free surfaces is negligible and change in the x-position of the contact node is small (order of 10^{-3}). The tests were performed for a base case of downstream pressure of 70, Capillary number of 0.02, Elasticity number of 0.002, contact angle of 90^{o}, and Elastic capillary number 10. Navier slip coefficient $\beta = 0.00001$, slip length over 2 elements, and contact region $L_{CR} = 0.1$ are used for the simulations.

The elements required in different regions, namely, elements upstream of the contact node in x-direction, elements downstream of the contact node in x-direction, elements in the y-direction in solid and liquid phases were optimized to obtain convergence and then from these tests the number of elements required for the whole domain were determined. Then the number of elements and stretching were increased simultaneously in all directions to show convergence. A coarse mesh with 4 elements in the y-direction in both the solid and liquid were increased to 8 elements (base case) and then to 10 elements (refine mesh). While the number of elements were increased, the stretching in the x-direction upstream and downstream was changed such that the size of nearest neighboring elements adjacent to the contact node decreases by 50 % from the coarse mesh to base case and then by another 50% from the base case to the refine mesh. The elements adjacent to the contact node are fixed and hence, their sizes do not change with refinement. There is a change in the dynamic contact line position of the order of 10^{-2} for a change from coarse mesh to base case mesh and then a change in the order of 10^{-3} in the contact line position for a change from base case to refine mesh. The solid free surface, liquid/vapor free surfaces, contours of pressure, displacements and velocity fields are compared to show convergence. Figures 12a-12b show a comparison of liquid/vapor free surface and solid free surface for all three meshes. It can be seen that there is a negligible change in the solid free surface and liquid/vapor free surface between base case and refine mesh. Figure 13 shows a comparison of contours for pressure fields between base case and refined case. The pressure field varies linearly at distances far from the contact line and the pressure contours predicted using the base case and refined meshes match. Close to the contact line there is small deviation in the contour shapes. Horizontal velocity field contours show a slight deviation near to the contact line but in the far field contours match, vertical displacement; vertical velocity and horizontal displacement field contours almost lie on one another between base case and refined case. After optimizing the elements in different regions and comparing the free surfaces and contours it has been concluded that 12 elements in x-direction with $h = 1.33$ on the solid/liquid side, 6 elements in x-direction with $h = 0.46$ on the solid/vapor side, 8 elements in y-direction of liquid and solid are sufficient to get a converged solution with respect to stretching and elements.

1.4.2 Comparison of spine and pseudo solid Mesh Motion Schemes

The two mesh motion schemes, pseudo solid and spines, were implemented in the solid domain but, pseudo solid mesh motion gives more distortion and hence, less accurate results. The distortions in the elements in the pseudo solid mesh are due to shearing and extension near the contact line as the contact line moves. Figure 14 shows the meshes at the limits of convergence for the mesh motion schemes. In the liquid domain, pseudo solid mesh motion has been used for all the results in this paper. The trends for the location of dynamic contact line with change in elasticity number from both the mesh motion schemes are same as seen from Figure 15. The predicted dynamic contact line x-position with the pseudo solid method is slightly higher than that of spine method. This difference is due to the elemental distortions in the pseudo solid mesh motion near the contact line. The y-position from both the mesh motion schemes is almost the same as shown in Figure 15. The elements are less distorted (Figure 14) with the spine method in the solid domain than with the pseudo solid method and also wider range of convergence of the code is obtained. The spine method in the solid is used for all the results in the remainder of the paper.

1.5 RESULTS

1.5.1 *Base Case for Wetting on a Flexible Substrate*

Figures 16, 18-20 display contour plots of pressure, velocity and displacement fields for downstream pressure of 70, Capillary number of 0.02, Elasticity number of 0.002, contact angle of 90^o and Elastic capillary number of 10.

Figure 16 shows the contours of pressure fields in the solid and liquid domains near the contact line. The pressure contours for the solid and liquid domain match at the downstream end, as there is negligible displacement in the vertical direction even though the solid is sheared there. Hence, the pressure in the solid is equal to the pressure in the liquid near the outflow plane and both vary linearly consistent with fully developed flow. Near the contact node there is a low-pressure region in both the solid and liquid phases. The pressure in the solid near the contact node is less than that of the liquid because the solid is in tension there due to the action of liquid/vapor surface tension pulling upward at dynamic contact line. The pressure variation is one-dimensional (along the x-direction) towards the outflow plane. Close to the free surface near the dynamic contact line, liquid turns around and hence pressure variation is two-dimensional there. Figure 17 shows that the pressure in the solid and liquid goes through a minimum at the contact line and then increases to the downstream almost linearly for most of the domain along the solid/liquid interface. Close to the contact line, pressure in the solid deviates from linear variation. Figure 18 shows the contours of horizontal velocity field in the liquid domain and vertical displacement field in the solid domain near the contact line. The horizontal velocity is zero at the contact node and rises to solid velocity through the Navier slip condition (equation (15)) over the slip length. After the slip length, the velocity of the liquid is equal to that of the solid because of the no slip condition. Variations in the horizontal

velocity at the solid surface are related to the gradient of the vertical displacement in the solid:

$$v_{L,x} = \left[1 - \frac{\partial v}{\partial y}\right] V_{S,x} \tag{40a}$$

Likewise the vertical fluid velocity along the interface is also related to the slope of the interface.

$$v_{L,y} = \frac{\partial v}{\partial x} V_{S,x} \tag{40b}$$

This equation was derived from equation (17). A maximum in vertical displacement of the solid occurs at the contact node because of the line force pulling the contact line upwards and reducing the gap size. The downstream end of the liquid domain corresponds to fully developed flow and the vertical displacement is zero.
Figure 19 shows the contours of vertical velocity field in the liquid domain. The vertical velocity in liquid is zero for most of the domain except near the upstream end where the fluid turns around to flow downstream. At the contact node vertical velocity is zero. Figure 20a shows the horizontal displacement field in the solid domain near the contact line. Horizontal displacement field contours show that near the downstream region of the contact node, solid is sheared towards the contact node because of the shear forces from the liquid and line force. Upstream of the contact node, solid is sheared towards the contact node because of the line force pulling the solid. Figure 20b shows the horizontal displacement varying along the substrate thickness where the solid is getting sheared along the solid/liquid interface. At the outflow plane, the horizontal displacement is parabolic as a result of shear forces and pressure forces acting there. Close to the contact line, the solid displacement is zero at the bottom of the solid and the displacement of the solid at the surface is resultant of line force, shear forces from the liquid and the pressure forces. The displacement at the surface close to the contact line comes out to be higher than that at the outflow plane because of line force. Displacements decay to zero at the inflow plane of the solid.

1.5.2 *Analytical Model for the Dynamic Contact Line Location for Rigid Solid*
To analyze the motion of dynamic contact line, we have derived an analytical model for the location of the dynamic contact line for rigid solid based on Higgins and Scriven [16]. Figure 21 depicts the domain and geometry of the analytical model. A comparison of the analytical and the finite element models is shown in Figure 23. The assumptions of the model are that the solid is rigid, the meniscus is an arc of circle and the pressure is a linear function of distance along the substrate.

$$P_{FS} = P_{down} + \left(\frac{\partial P}{\partial x}\right)_{down} (x_{DCL} - x_{down}) \tag{41}$$

Where P_{FS} is the pressure at the meniscus, P_{down} is the pressure at the downstream end, $\left(\frac{\partial P}{\partial x}\right)_{down}$ is the pressure gradient at the downstream end and is equal to $\frac{6\mu v_s}{h_L^2}$, x_{DCL} is the location of the dynamic contact line and x_{down} is the location of the downstream end.

The liquid pressure at the meniscus comes from the capillary pressure across the curved meniscus:

$$P_{FS} = \frac{s_{LV}}{R} \tag{42}$$

Where R is the radius of curvature.

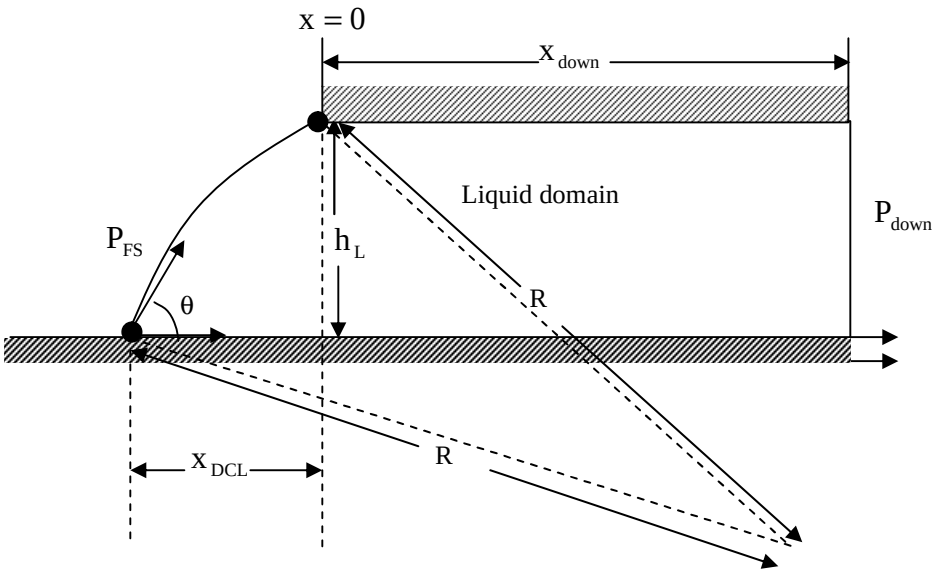

Figure 21. *Schematic of computational domain for analytical model of dynamic wetting on rigid substrate moving with a velocity* $V_{S,x}$ *and liquid/vapor free surface making an angle q with the solid.*

The radius of curvature R is related to the dynamic contact line position by:

$$R = \frac{-(h_L^{\,2} + x_{DCL}^{\,2})}{2(h_L \cos? - x_{DCL} \sin?)} \tag{43}$$

Equations (41)-(43) are combined to develop an equation relating the downstream pressure and the location of dynamic contact line:

$$P_{down} + \frac{6mv_s(x_{DCL} - x_{down})}{h_L^{\,2}} + \frac{2s_{LV}(h_L \cos? - x_{DCL} \sin?)}{(h_L^{\,2} + x_{DCL}^{\,2})} = 0 \tag{44}$$

1.5.3 *Analytical Model for the Dynamic Contact Line Location for Flexible Solid*
To account for substrate flexibility in the analytical model presented above, vertical displacement of the solid at the contact line modifies the geometric relationship for

meniscus curvature (equation (45)). As a simple approximation for a flexible solid, the solid at the contact line is assumed to behave as a spring as shown in Figure 22. The deformed gap at the contact line is assumed to follow Hooke's law:

$$h'_L = h_L\left(1 - \frac{s_{LV}\sin?}{Gx}\right) \qquad (45)$$

Where x is a constant determined from numerical experiments with static wetting such that x = 2.333.

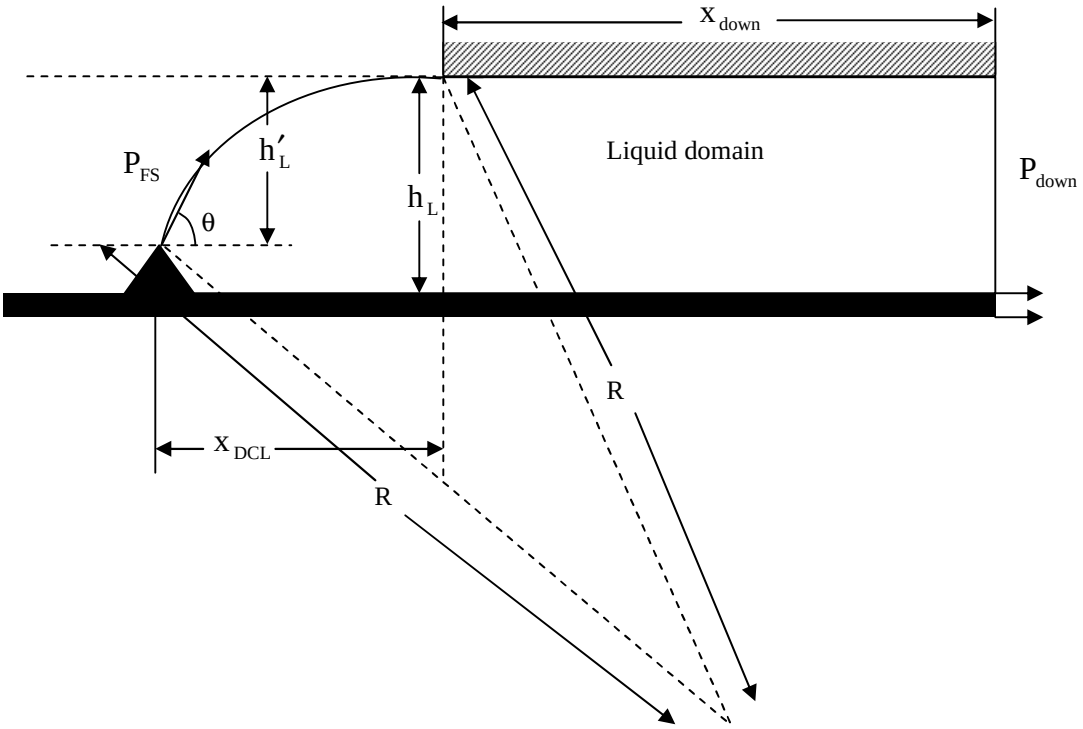

Figure 22. *Schematic of computational domain for analytical model of dynamic wetting on flexible solid moving with a velocity* $V_{S,x}$ *and liquid/vapor free surface making an angle q with the bisecting plane.*

For simplicity, the substrate deformation is assumed only to affect the relationship for curvature and does not affect the pressure profile in the gap. Equation (44) and (45) gives the following model for the flexible solid:

$$P_{down} + \frac{6mv_s(x_{DCL} - x_{down})}{[h_L]^2} + \frac{2s_{LV}\left(h_L\left(1 - \frac{s_{LV}\sin?}{Gx}\right)\cos? - x_{DCL}\sin?\right)}{\left(\left[h_L\left(1 - \frac{s_{LV}\sin?}{Gx}\right)\right]^2 + x_{DCL}{}^2\right)} = 0 \qquad (46)$$

This equation relates downstream pressure and dynamic contact line position for a flexible solid.

1.5.4 *Study of Variation of Dynamic Contact Line with Downstream Pressure, Capillary Number, Contact Angle for Rigid and Flexible Solids*

The dynamic wetting line position variation with different parameters for rigid solid such as downstream pressure, Capillary number and Contact angle for rigid solid are presented in Figures 23, 25, 27 and 29. The results show that increase in downstream pressure moves the contact line away from the gap (upstream), decrease in capillary number pushes the contact line towards the gap (downstream) if the meniscus is convex from the vapor side, increase in contact angle pushes the contact line towards the gap (downstream). Figure 23 depicts the comparison from analytical and FEM models for the variation of dynamic contact line position with downstream pressure for rigid solid. There is a good qualitative agreement between the analytical and FEM results for rigid solid as shown in Figures 23. Both the models predict the same trends that increase in downstream pressure moves the contact line away from the gap. The slope of the curve deviates from linearity for low or high pressures as the dependence of radius of curvature on dynamic contact line position becomes non-linear as seen from the analytical model (Equation (44)).

Figure 25 shows the variation of dynamic contact line position in FEM model with downstream pressure for a rigid solid. With increase in downstream pressure, with all the other parameters constant, the pressure in the gap goes up. In order to balance the pressure in the liquid and the pressure drop across the meniscus, the meniscus increases the length of the gap pushing the contact node away from the gap (upstream) and similarly when the downstream pressure is decreased, it moves the contact node towards the gap (downstream). The meniscus changes its shape from concave to convex from vapor side as the downstream pressure is increased.

Figure 27 shows the variation of dynamic contact line position with capillary number for a rigid solid. The trends for the variation of the dynamic contact line position with capillary number are different depending on the shape of the meniscus. With decrease in capillary number, all the other parameters constant, surface tension goes up. With increase in surface tension, the pressure drop across the liquid/vapor free surface goes up. In order to balance the pressure in the liquid and pressure drop across the meniscus, the length decreases by pushing the contact node towards the gap (downstream) if the meniscus is curved convex from the vapor side. If the meniscus is curved concave from the vapor side, the physics remains the same but the meniscus moves upstream. As the surface tension increases, the meniscus shape becomes flat due to the increase in radius of curvature.

Figure 29 shows the variation of dynamic contact line position with contact angle for a rigid solid. With the increase in contact angle, the free surface should decrease the radius of curvature and hence the pressure near the free surface goes up hence, the meniscus decreases the length in order to balance the pressure and the converse is true when the contact angle is decreased. The analytical model for rigid solid gives a good qualitative agreement for the variation of capillary number and contact angle.

Figure 24 depicts the predictions of dynamic contact line location for a flexible solid from the analytical and finite element methods. As the downstream pressure is increased,

the contact line moves away from the gap and as the downstream pressure is decreased, the contact line moves into the gap. The meniscus changes its shape from concave to convex from vapor side as the downstream pressure is increased as shown in Figure 26. There is good qualitative agreement between the analytical and FEM models. The physics remains the same as that of rigid solid at constant elasticity number. As the downstream pressure is increased, the pressure in the liquid increases and the meniscus balances the pressure drop across the meniscus and the pressure in the liquid by lengthening the gap and the converse is true when the pressure is decreased. The quantitative agreement between the analytical and FEM models is not good because of the assumptions of free surface to be an arc of circle and pressure gradient in the liquid domain to be a constant all the way till the meniscus, which is not valid as shown in Figure 17.

The trends and the physics for the variation of dynamic contact line with capillary number and contact angle at constant elasticity number remain the same as that of rigid solid. The meniscus moves downstream with decrease in capillary number when the meniscus is curved convex from the vapor side as shown in Figure 28 and moves upstream with decrease in capillary number when the meniscus is curved concave from the vapor side. The meniscus moves upstream with decrease in contact angle. The analytical model gives a good qualitative agreement for the variation of capillary number and contact angle at a constant elasticity number.

1.5.5 *Effect of Substrate Stiffness on the Position of the Dynamic Contact Line with Variation in Downstream Pressure, Capillary Number and Contact Angle*

In general, the variation of the dynamic contact line position with downstream pressure, capillary number and contact angle for constant elasticity number follow the same trends qualitatively as that of rigid solid as discussed in last section. The variation of dynamic contact line position with substrate stiffness for constant downstream pressure, capillary number and contact angle is displayed in Figure 30. With increase in flexibility of the solid, the displacement of the contact node increases in the vertical direction as a result of increase in strain as shown in Figure 30. If the meniscus is concave from the vapor side and for lower contact angles, the decrease in gap results increase in pressure near the meniscus and hence, the meniscus moves upstream and away from the gap to balance the pressure in the liquid and pressure drop across the meniscus. The analytical model supports this trend for all elasticity numbers. The higher the flexibility of the solid, the more the contact line moves upstream as seen from the results in Figure 30b. Figure 31 show the mesh and the contact node moving upstream as the elasticity number is increased. When the meniscus is curved convex from the vapor side and for lower contact angles, the meniscus moves upstream for lower elasticity numbers and then downstream for higher elasticity numbers as shown in Figure 30a. The initial trend of the meniscus moving upstream is not supported by the analytical model which could be due to the fact that stresses from the liquid are neglected, which could be important at higher pressures. At higher elasticity numbers, the stress from the line force increases and hence, it dominates over the stress from the liquid and hence, the trends from analytical model and FEM match.

In Figure 25 the variation of dynamic contact line with substrate flexibility and downstream pressure for finite element method is shown. The contact line moved

upstream (away from the gap) for lower elasticity numbers and for lower contact angles at constant downstream pressure. This behavior for lower elasticity numbers is observed in the analytical model only when the meniscus is curved concave from the vapor side. This could be due to neglecting the stresses from the liquid in the analytical model, which could be important at higher pressures. As the flexibility of the solid is increased, the pressure near the meniscus increases due to the decrease in the gap and so the meniscus balances the pressure drop across the meniscus and the pressure in the liquid by moving upstream.

With decrease in capillary number, the line force increases and hence the vertical displacement of the contact node increases which results in the decrease of the gap and hence the pressure near the meniscus in the liquid goes up. If the meniscus is curved concave from the vapor side and for lower contact angles, the meniscus balances the pressure in the liquid and pressure drop across the meniscus by moving upstream and away from the gap as seen from the Figure 27b. The analytical model supports this trend. For constant capillary number, lower elasticity numbers and lower contact angles, the contact line moves further upstream if the meniscus is curved convex from the vapor side which is opposite of the trend given by the analytical model. This could be the effect of stresses from the liquid where they tend to push the contact node upstream. This effect is seen in the Figure 27a.

Figure 29 depicts the predictions of variation of dynamic contact line position with elasticity number and contact angle. For higher contact angles, the meniscus moves downstream with respect to the rigid solid with increase in flexibility (lower elasticity numbers) and the converse is true for lower contact angles as shown in Figure 28. The mechanism is similar to the other parameters.

The trend with change in elasticity number is supported by the analytical model at all elasticity numbers if the meniscus is convex from the vapor side; higher contact angles and if the meniscus is concave from the vapor side; lower contact angles and at higher elasticity numbers at all conditions.

1.6 CONCLUSIONS

This paper presents a finite element formulation for solving dynamic wetting on flexible solids with application to the upstream end of slot coater as the test problem. The challenge involved in this model is coupling the fluid and solid mechanics and taking into account the motion of dynamic contact line across the flexible substrate. There are two singularities that arise because of line force acting on the solid and a double valued fluid velocity arising in the liquid. The singularity in the solid is relieved by applying the line force over a finite contact region and the singularity in the liquid is relieved by applying the Navier-slip condition. The boundary conditions at the contact node involve applying two momentum balance conditions on the solid, a kinematic condition and a no penetration condition on the liquid velocity, contact angle condition and Lagrangian motion on the mesh displacements.

The parametric studies have shown that the pressure at the outflow, capillary number, contact angle and substrate stiffness affect the motion of the contact line. At constant elasticity numbers, increase in downstream pressure pushes the contact line away from the gap, decrease in capillary number moves the contact node away from the

gap if the meniscus is curved concave from the vapor side and increase in contact angle pushes the contact node into the gap.

The substrate stiffness has an effect on the motion of the contact line. The results have shown that at higher substrate stiffness at the same operating parameters, the contact line is pushed into the gap if the meniscus is convex from the vapor side and decreases the gap width by moving vertically. Conversely, the contact line moves upstream and away from the gap when the meniscus is curved concave from the vapor side. This paper provides a new formulation that can be applied to various applications, which involve flexible solids in contact with liquids and three phase wetting lines. There are also many industrial processes which could benefit from this model, such as roll coating, flexible blade coating and in studying flow though porous media in recovery of oil in rocks.

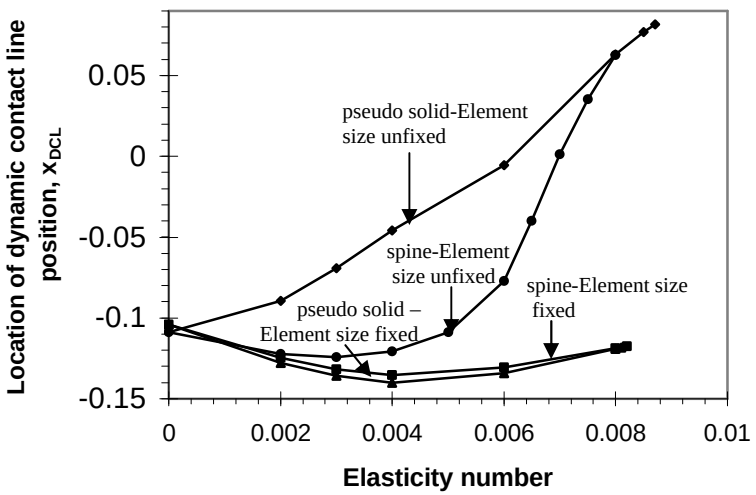

Figure 11. *Comparison of location of dynamic contact line as a function of Elasticity number for spine mesh motion and Pseudo solid mesh motion for constant contact region versus variable contact region. Downstream pressure = 70, contact angle = 90^o and Ca = 0.02.*

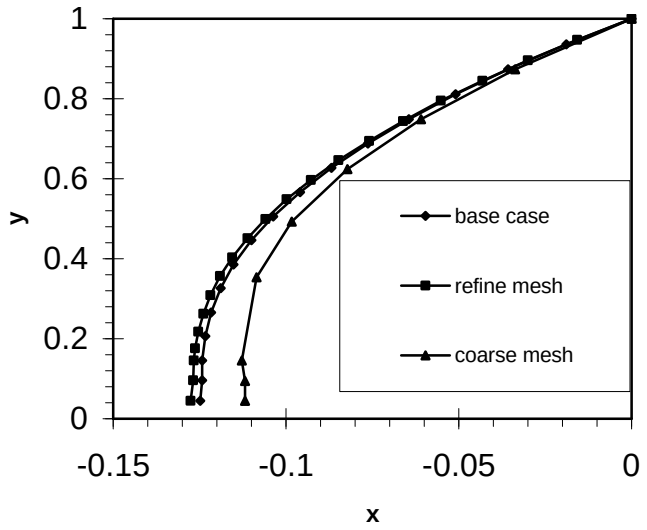

(a)

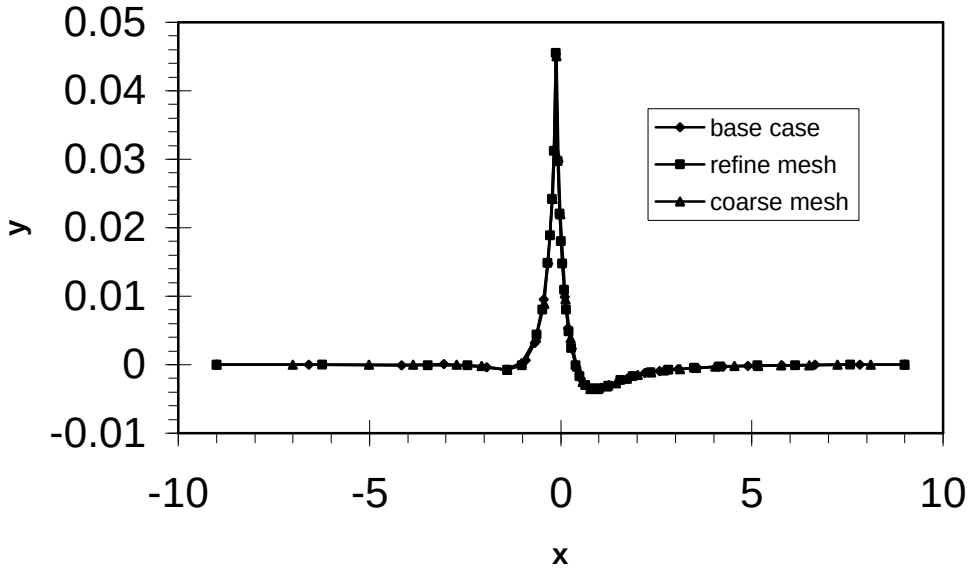

(b)

Figure 12. *Mesh refinement study. Comparison of (a) shape of liquid-vapor free surface and (b) shape of solid-liquid free surface at three levels of mesh refinement. The contact angle is 90°,* $Ca_{ESV} = Ca_{ESL} = 10$, *Ca = 0.02,* $E_s = 0.002$ *and downstream pressure = 70 are used for this comparison.*

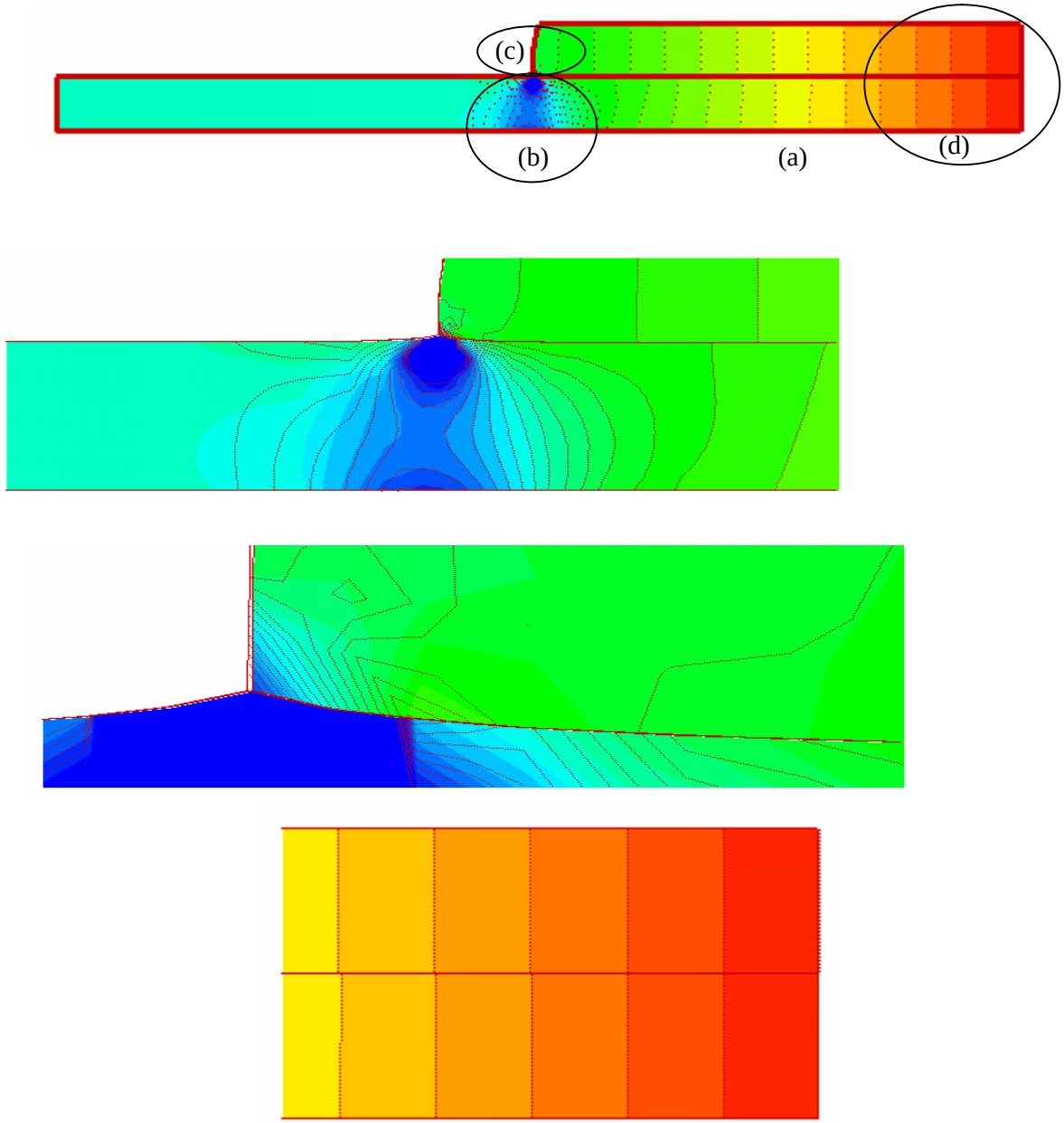

Figure 13. *Comparison of contour plot of pressure field (a) for full domain (b) solid domain close to the contact line (c) liquid domain close to the contact line (d) close to the outflow plane at two levels of mesh refinement with solid contours for base case and dotted contours for refined mesh. The contact angle of* 90^o, $\mathrm{Ca}_{\mathrm{ESV}} = \mathrm{Ca}_{\mathrm{ESL}} = 10$, $E_s = 0.002$, $Ca = 0.02$ *and downstream pressure = 70 are used for this comparison. The minimum pressure contour level was set at –30, maximum pressure contour level was set at 70 and the number of levels was set to 26.*

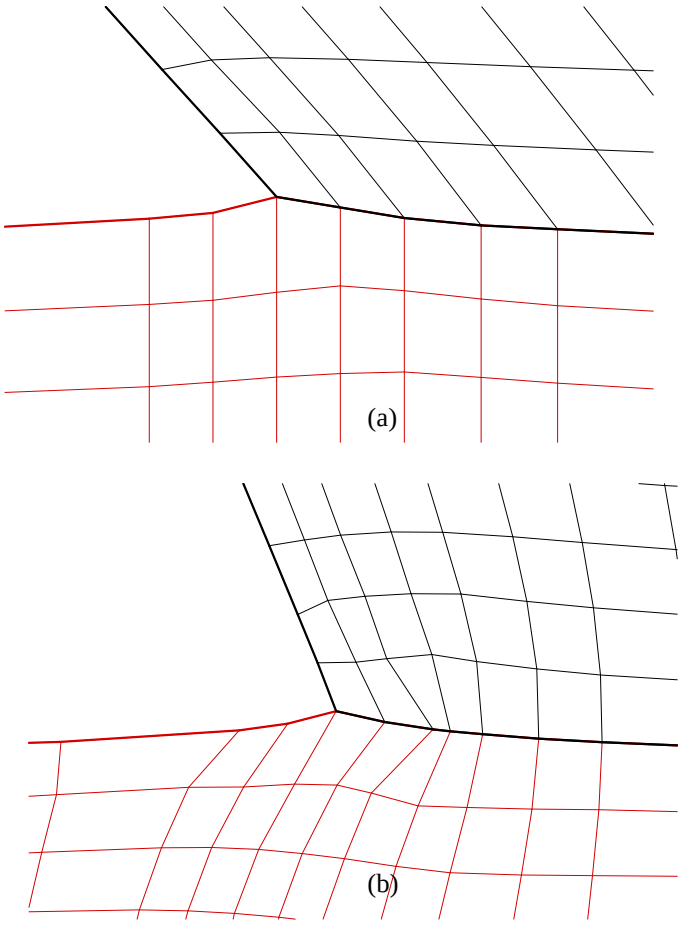

Figure 14. *Shape of mesh near the dynamic contact line position at downstream pressure = 50, Es = 0.002 and Ca = 0.02 for (a) spine mesh motion – contact angle – 127^o and (b) pseudo solid mesh motion – contact angle - 109^o.*

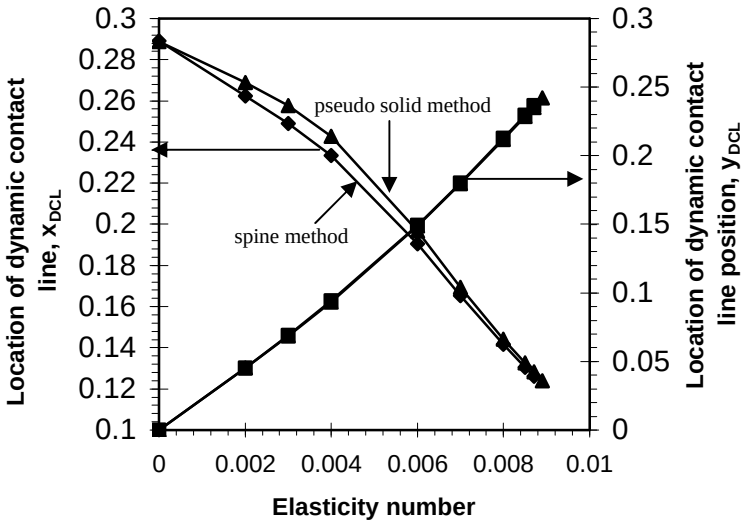

Figure 15. *Comparison of location of dynamic contact line as a function of elasticity number for spine mesh motion versus pseudo solid mesh motion for downstream pressure = 30, contact angle = 90^o and Ca = 0.02.*

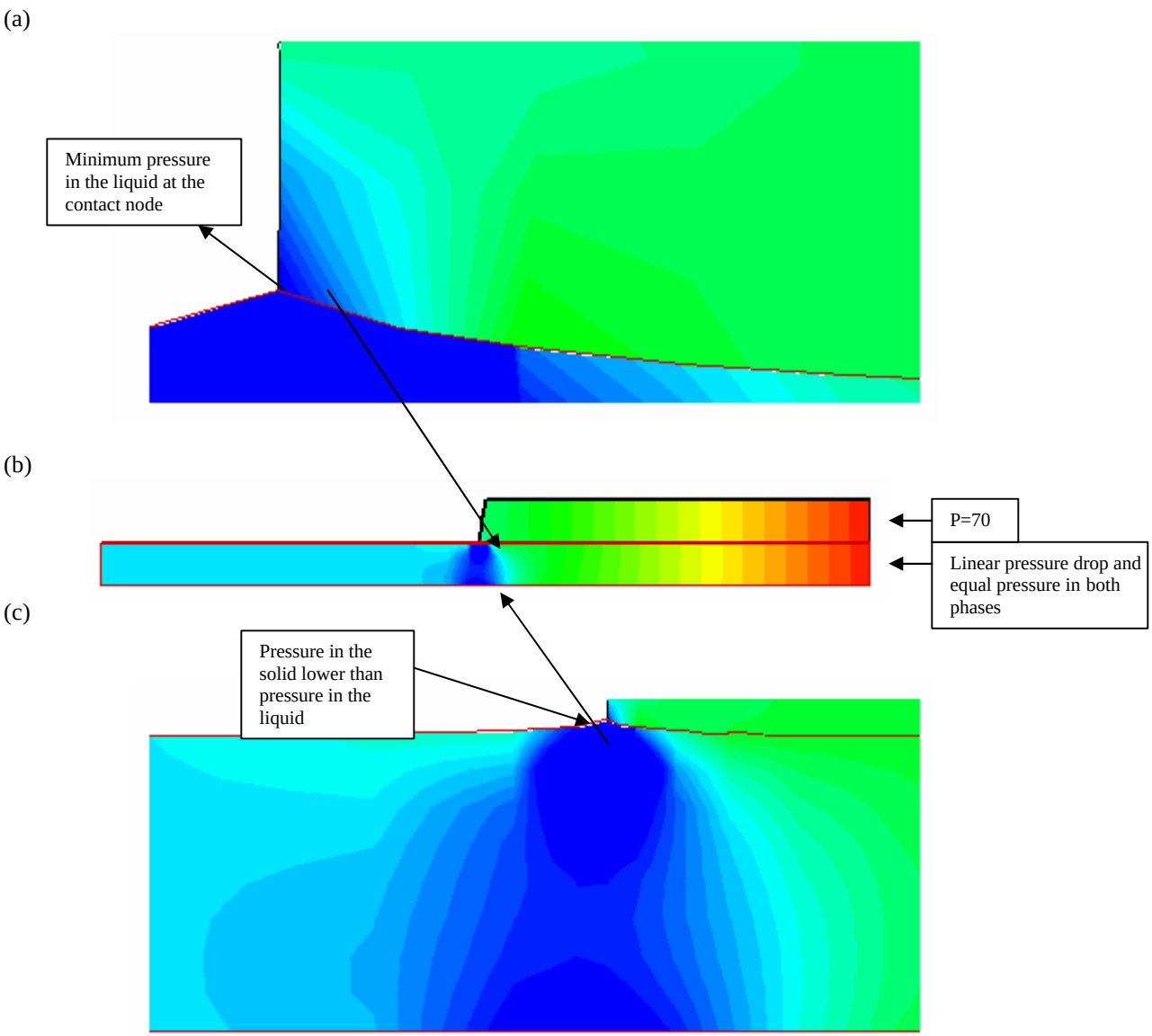

Figure 16. *Contour plots of pressure field for base case conditions: (a) liquid domain (b) full domain, and (c) close to the contact node in the solid with downstream pressure = 70, contact angle = 90^o, Es = 0.002 and Ca=0.02. The maximum and minimum contour levels are at 70 and –20 with the number of levels 31.*

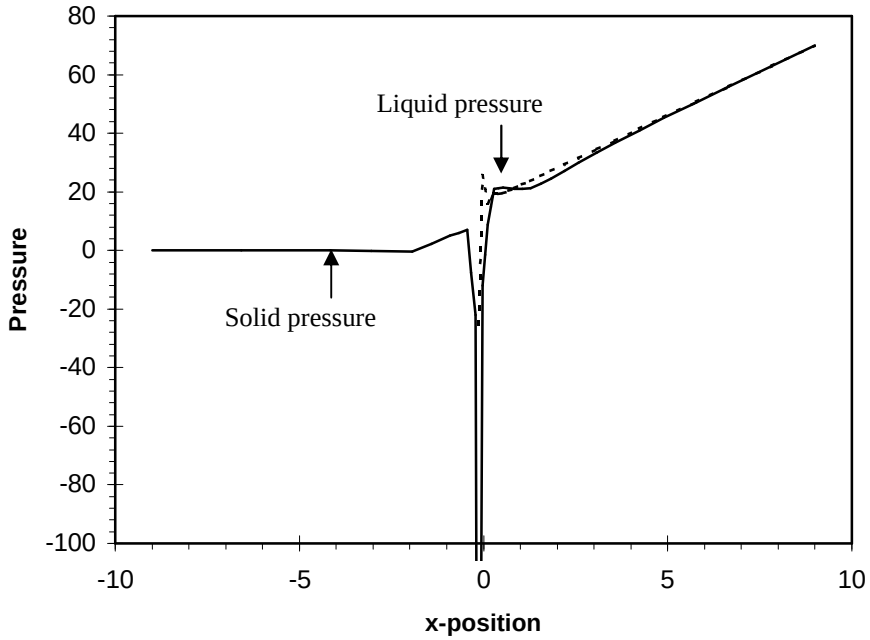

Figure 17. *Variation of pressure in solid and liquid as a function of x-position along the solid surface for base case conditions. Downstream pressure = 70, E_s = 0.002, contact angle = 90^o and Ca = 0.02. Solid pressure at dynamic contact line drops to about –300.*

(a)

(b)

(c)

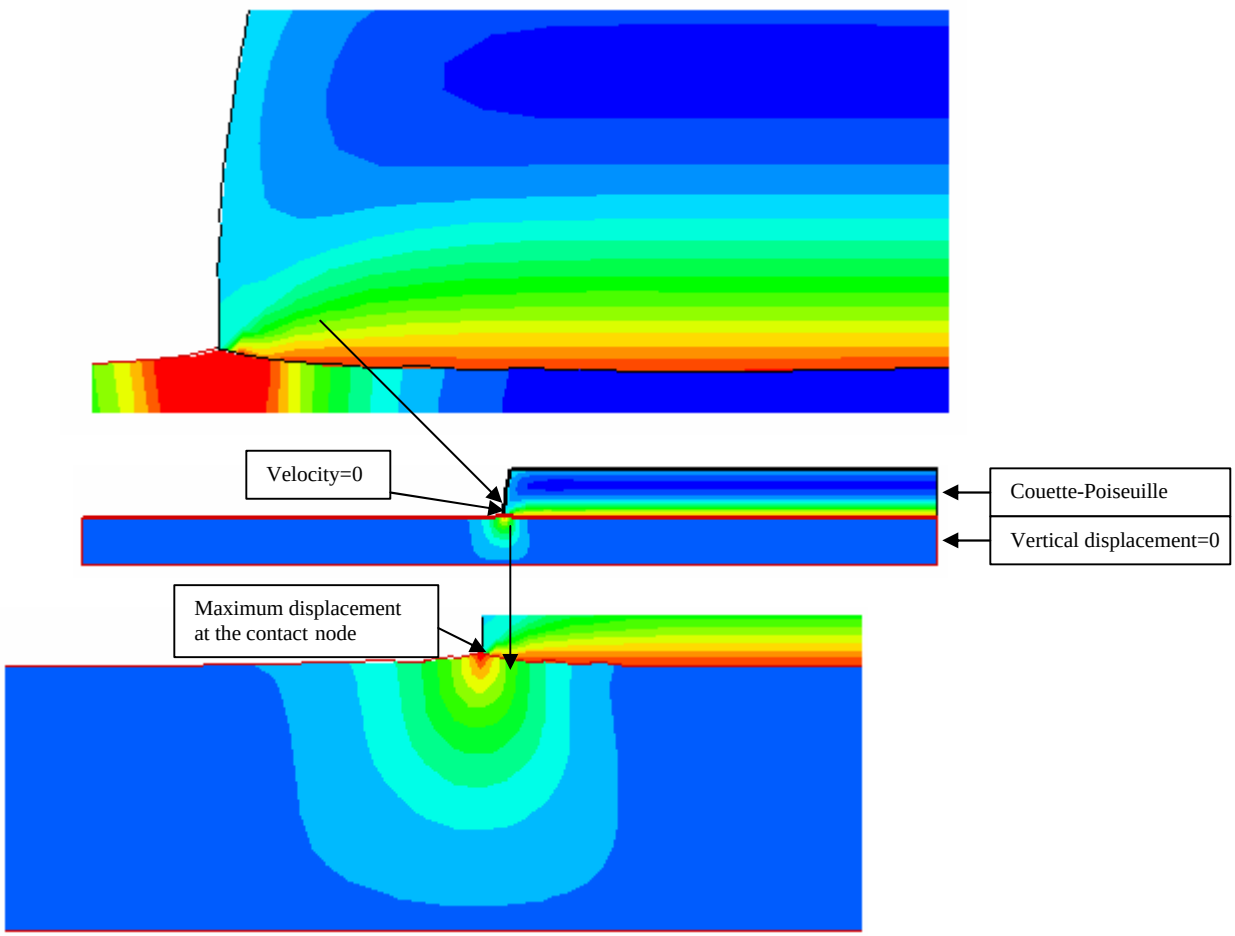

Figure 18. *Contour plots of horizontal velocity in liquid and vertical displacement in solid for base case: (a) close to the contact node in liquid, (b) for the full domain, and (c) close to the contact node in the solid. Downstream pressure = 70, contact angle = 90^o, E_s = 0.002 and Ca = 0.02. The maximum and minimum contour levels for velocity are at 1 and -0.3 with the number of levels 14 and for displacement are at 0.04 and -0.004 with the number of levels 11 respectively.*

(a)

(b)

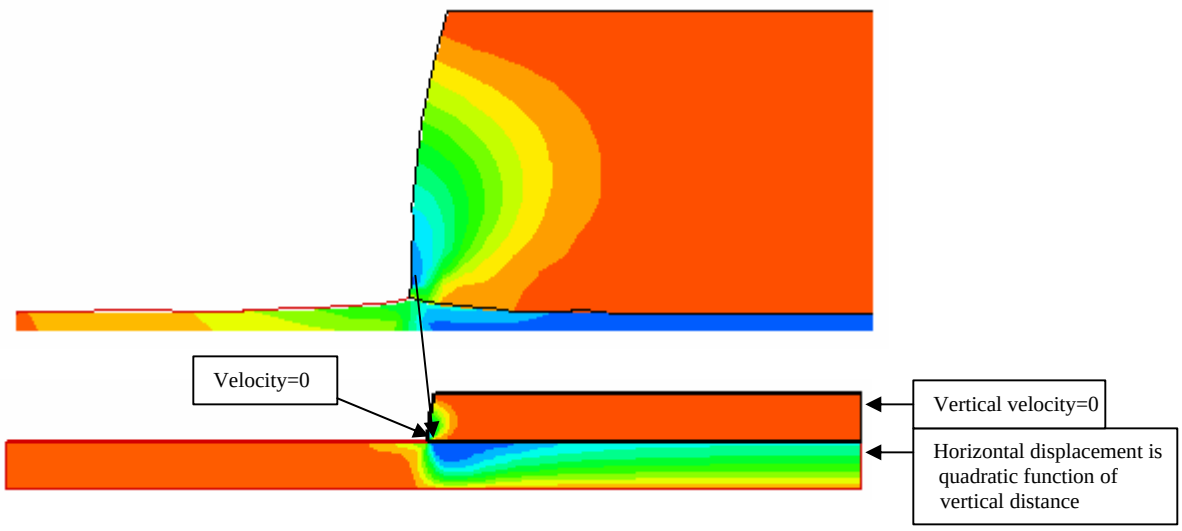

Figure 19. *Contour plots of vertical velocity in liquid and horizontal displacement in solid for base case: (a) close to the contact node in liquid (b full domain. Downstream pressure = 70, contact angle = 90^o, E_s = 0.002 and Ca = 0.02. The maximum and minimum contour levels for velocity are at 0.02 and -0.7 with the number of levels 13.*

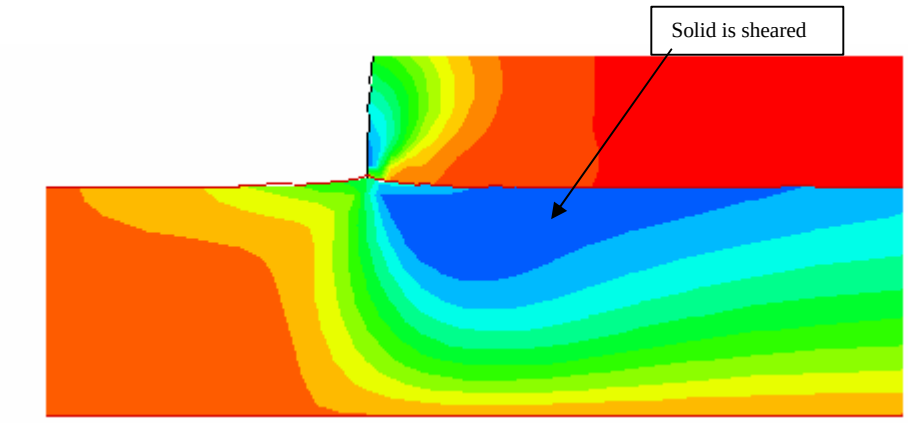

(a)

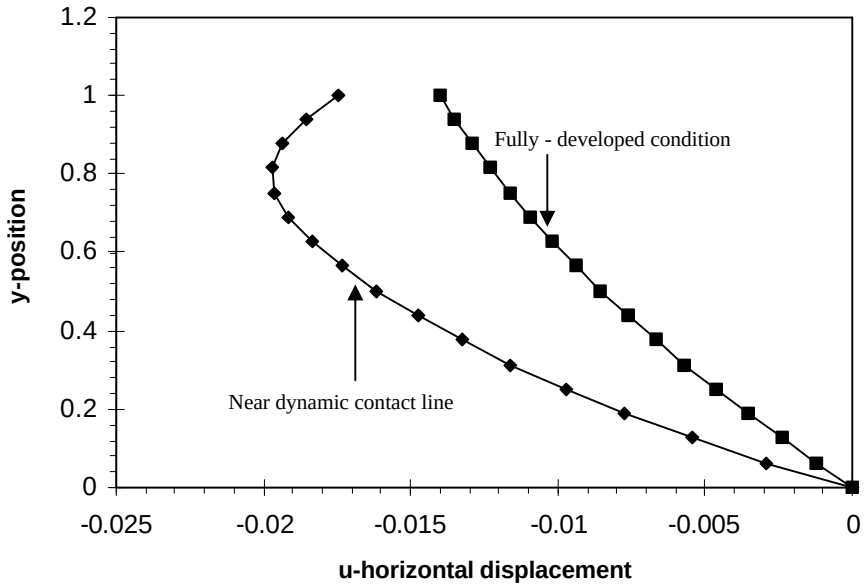

(b)

Figure 20. *Contour plot of (a) horizontal displacement in solid and vertical velocity in liquid close to the contact node in the solid and (b) Line plot of horizontal displacement through the substrate at an arbitrary x-position of 9.29 close to the dynamic contact line for base case. Downstream pressure = 70, contact angle = 90^o, E_s = 0.002 and Ca = 0.02. The maximum and minimum contour levels for velocity are at 0.02 and -0.7 with the number of levels 13 and for displacement are at 0.002 and -0.02 with the number of levels 11 respectively.*

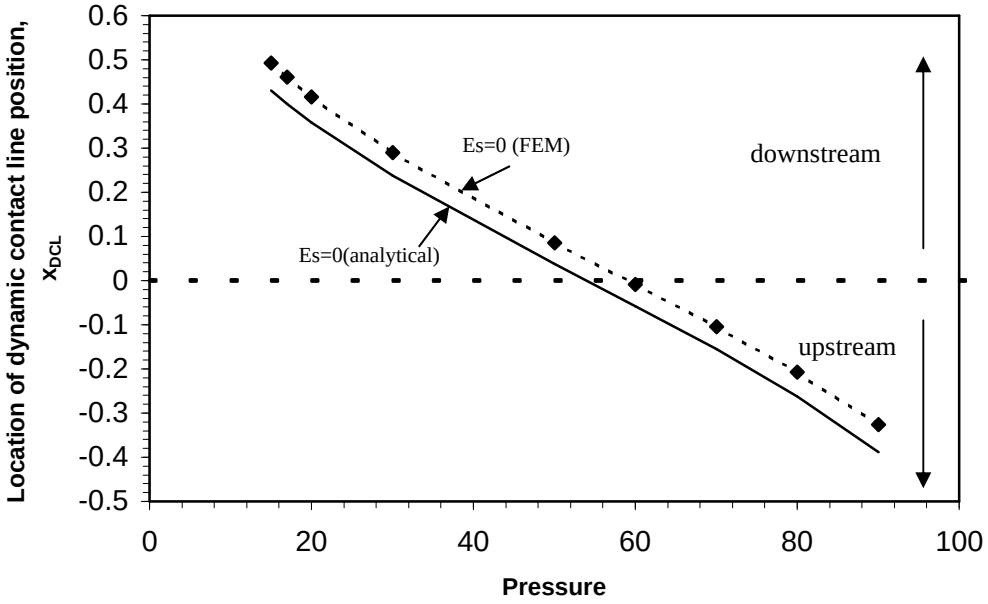

Figure 23. *x-position of the dynamic contact line as a function of downstream pressure at E_s = 0, contact angle = 90^o and Ca = 0.02 for analytical and finite element methods.*

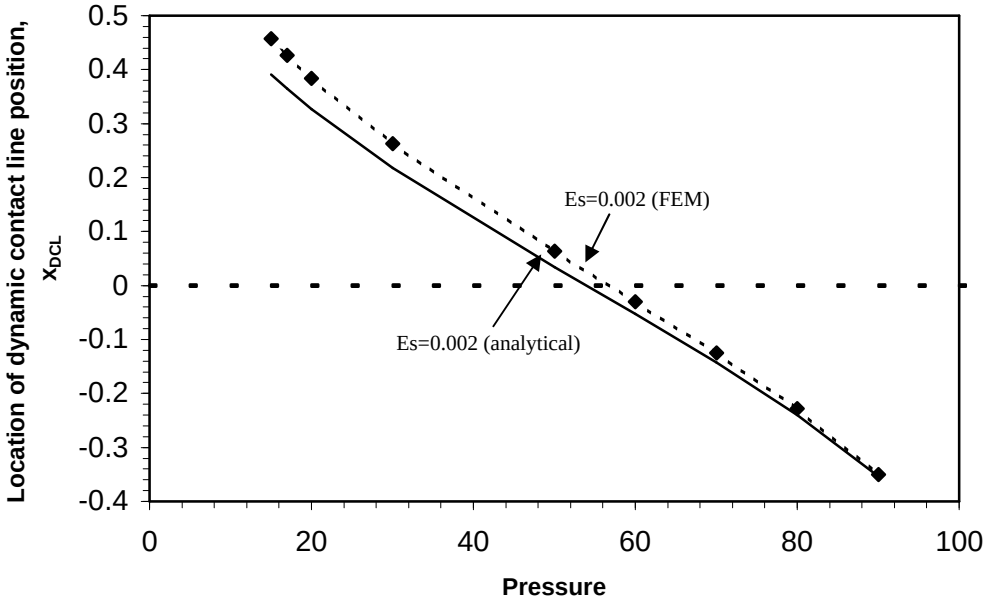

Figure 24. *x-position of the Dynamic contact line as a function of downstream pressure for E_s = 0.002, contact angle = 90^o and Ca = 0.02 for analytical and finite element methods.*

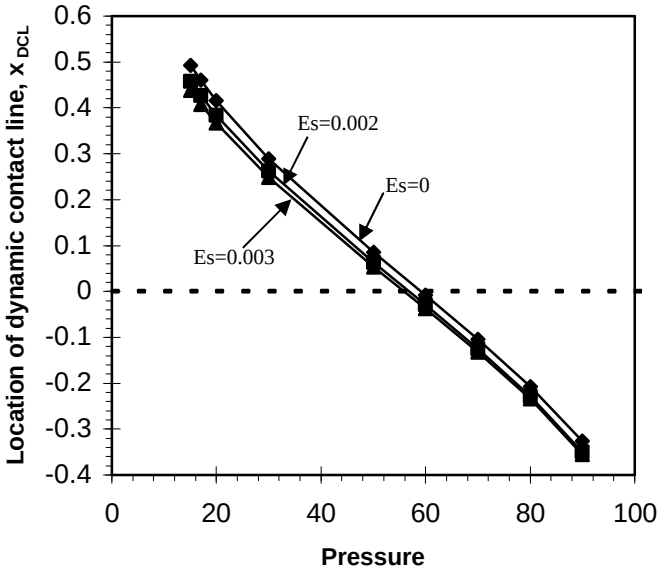

Figure 25. *Location of dynamic contact line as a function of downstream pressure for contact angle=90^o and Ca=0.02.*

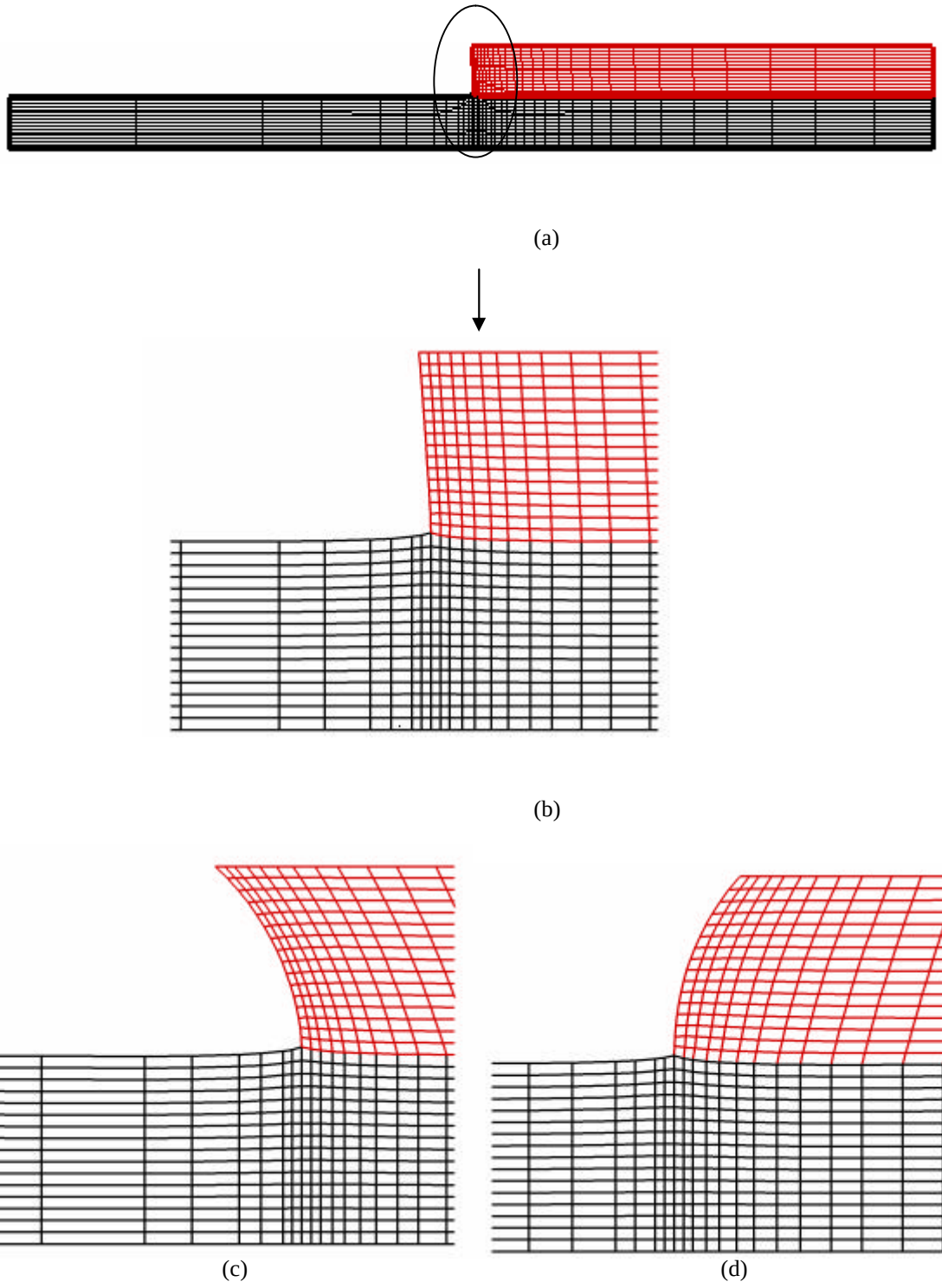

Figure 26. *Shape of the mesh for (a) full domain with downstream pressure = 50, near the contact node for (b) base case with downstream pressure = 50, (c) low downstream pressure with pressure = 15, and (d) high downstream pressure with pressure = 90, Es = 0.002, contact angle = 90^o, Ca = 0.02.*

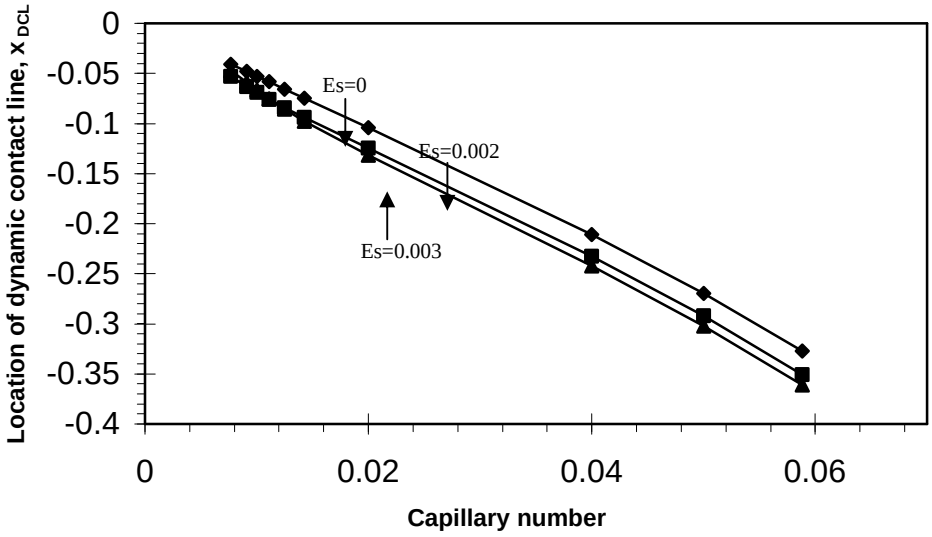

(a)

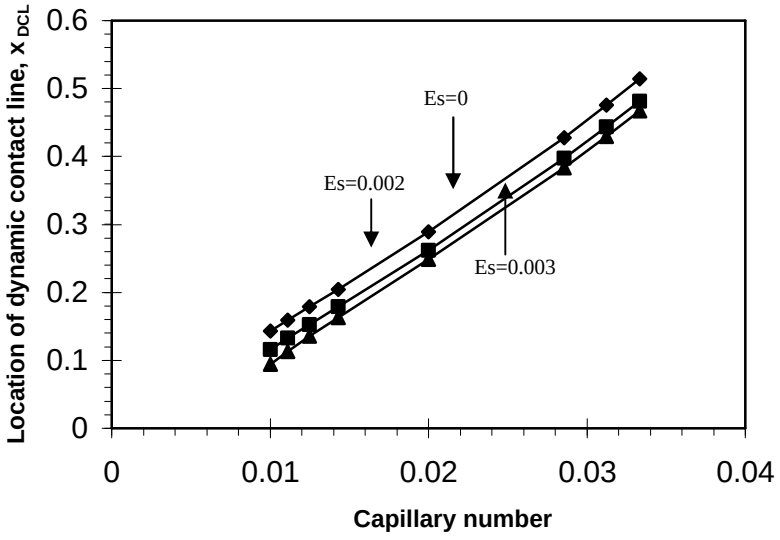

(b)

Figure 27. *Location of dynamic contact line as a function of capillary number for (a) high downstream pressure with pressure = 70 and (b) low downstream pressure with pressure = 30 and contact angle = 90^o.*

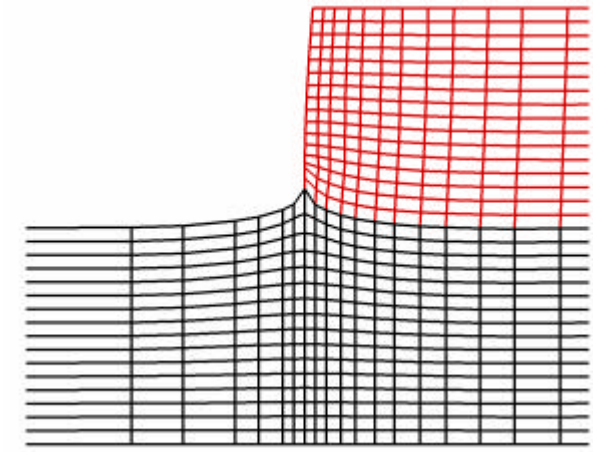

(a)

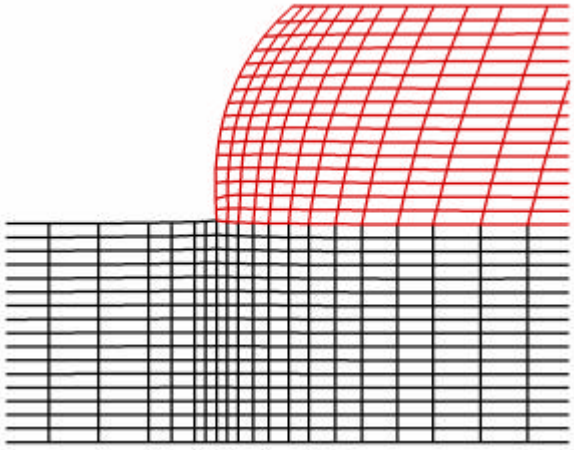

(b)

Figure 28. *Shape of the mesh near the contact node for (a) low capillary number with Ca = 0.0058, (b) high capillary number with Ca = 0.058, downstream pressure = 70, Es = 0.002, contact angle = 90^o.*

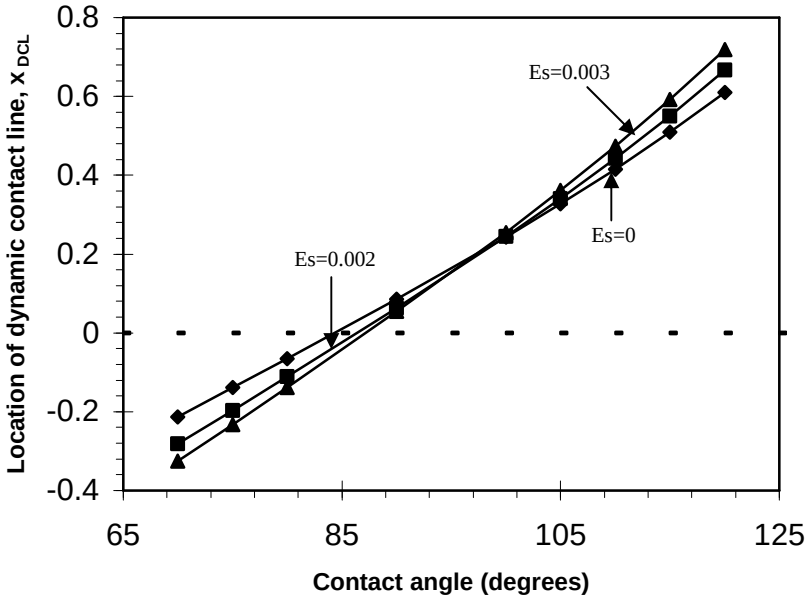

(a)

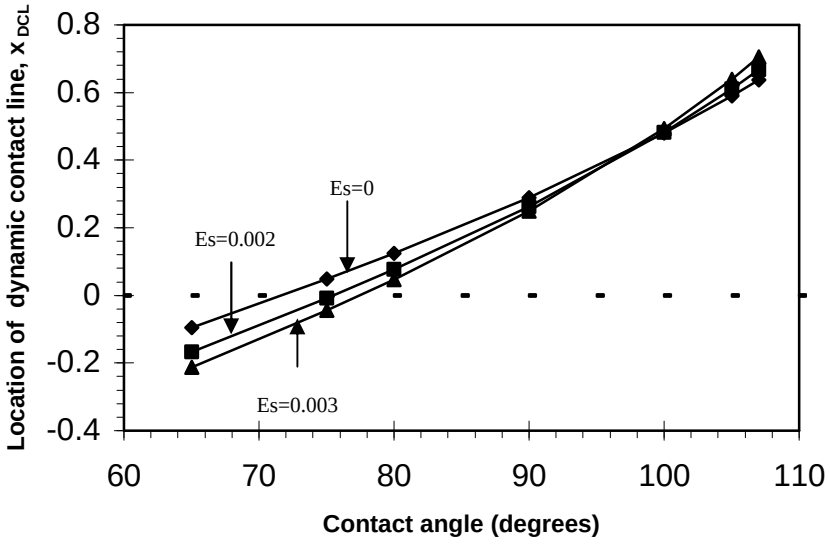

(b)

Figure 29. *Location of dynamic contact line as a function of contact angle for (a) high downstream pressure with pressure = 50 and (b) low downstream pressure with pressure = 30 and Ca = 0.02.*

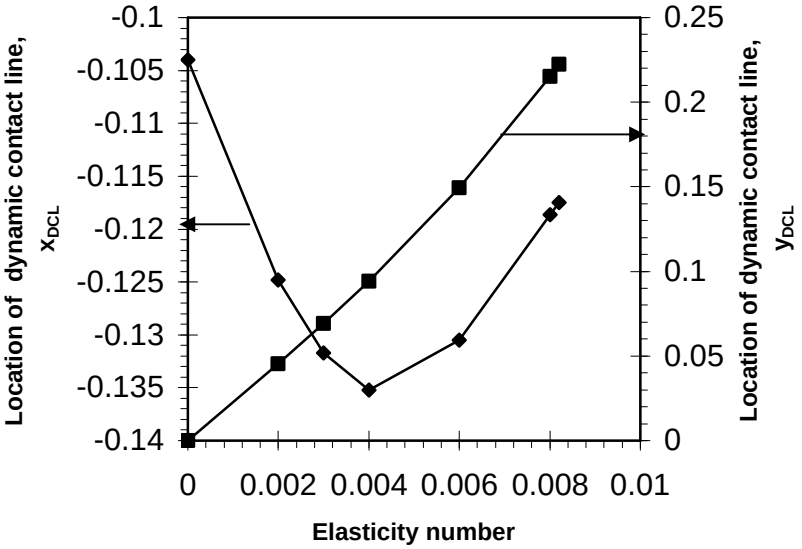

(a)

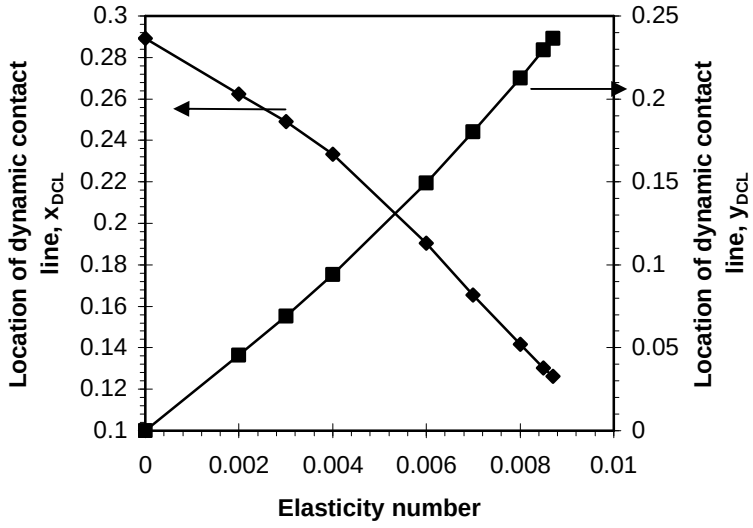

(b)

Figure 30. *Location of dynamic contact line as a function of elasticity number for (a) high downstream pressure with pressure = 70 and (b) low downstream pressure with pressure = 30, contact angle = 90^o and Ca = 0.02.*

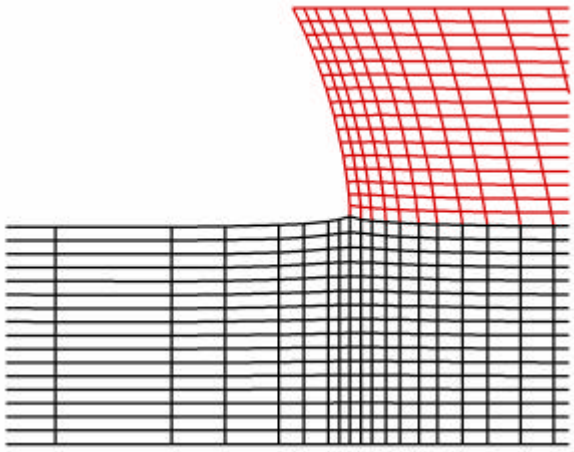

(a)

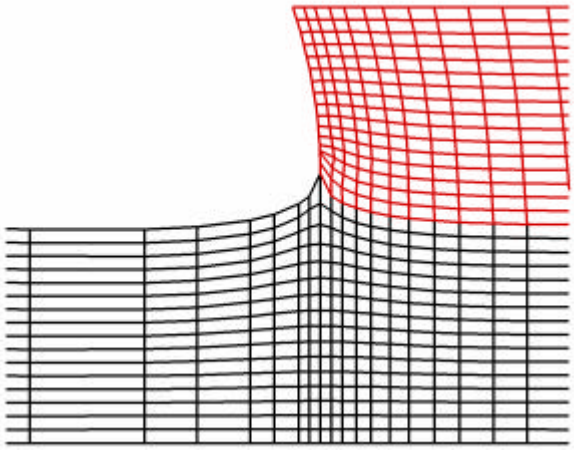

(b)

Figure 31. *Shape of the mesh near the contact node for (a) semi-flexible solid with Es = 0.002, (b) flexible solid with Es = 0.0087, downstream pressure = 30, contact angle = 90^o, Ca = 0.02.*

2. Wetting and penetration in deformable porous media

The transport properties of hygroscopic porous media, such as paper, are a strong function of the extent of swelling. Dry paper fibers exhibit a flat, ribbon-like shape. When the moisture content of paper rises water diffuses into paper fibers, which reduces the tension of condensed water in the lumen and reduces the strength of hydrogen bonds. Then, the lumen of the fiber expands and the morphology of individual paper fibers transforms from a ribbon-like shape to an elliptical cross-section. A single-fiber model has been developed to predict the change in cross-sectional shape of paper fibers during swelling and drying. The model balances elastic stresses in the fiber wall to a transmural pressure caused by the capillary pressure of condensed water in the lumen.

Macroscopic transport properties (e.g. effective diffusion coefficients) in porous media depend strongly on the morphology of the medium. Paper fibers are arranged randomly within the plane of the paper. An idealized unit cell structure has been developed to reproduce the key features of paper. The idealized unit cell contains layers of paper fibers with fibers in each layer parallel to each other and fibers in adjacent layers perpendicular to each other. The fiber cross-sections from the single-fiber model have been imported into the unit cell structure in order to predict effective diffusion coefficients and porosity for paper.

To predict the changes in microstructure of paper during drying and moisturization, a single-fiber deformation model has been developed. Wet paper fibers resemble thick-walled tubes and during processing (drying and calendaring), the thick-walled tubes collapse to a ribbon-like shape. This collapse is caused by capillary pressure of water in the lumen of the tube exerting tensile stresses on the tube wall. The single-fiber model balances elastic stresses in the fiber wall to a transmural pressure caused by the capillary pressure of condensed water in the lumen. The single-fiber model treats the fiber wall as an isotropic hyperelastic material. Deformation of the tube is predicted using Abacus, a commercial finite element package. With Abacus, it is possible to predict deformation of a tube from a nearly-elliptical cross-section to a ribbon-like geometry in which the lumen is essentially completely collapsed. The geometry of collapsed tubes from model matches qualitatively with observations of drying paper fibers. Experiments have also been conducted at Drexel (by a summer student in summer 2003) to observe the shape of tubes collapsing under negative (i.e. lower on inside) transmural pressures. The experiments and model both predict that the cross-section remains elliptical up to a critical value of the transmural pressure (normalized by the elastic modulus). At this critical pressure, the lumen collapses rapidly until opposite walls of the tube touch, and then the cross-sectional area of the tube plateaus.

The predicted fiber shapes from the single-fiber model have been used to predict macroscopic properties of paper using and idealized microstructural model. An idealized unit cell structure has been developed to reproduce the key features of paper. The idealized unit cell contains layers of paper fibers with fibers in each layer parallel to each other and fibers in adjacent layers perpendicular to each other. The fiber cross-sections from the single-fiber model have been imported into the unit cell structure. The unit cell

structure has been used to create a finite element mesh in FEMLAB to model transport within the inter-fiber pore-space. To predict effective diffusion coefficients, a water vapor concentration difference is imposed across the unit cell and the flux of water vapor is predicted by solving the diffusion equation within the inter-fiber pore-space. The model predicts that the effective diffusion coefficient decreases by about a factor of two between the wet and dry states. The porosity of the paper also decreases by about the same amount.

The results from this microstructural model of transport properties in paper will be used to predict drying and moisturization of paper coatings. The procedure used here to predict transport properties is not particularly complicated although it is computationally intensive because the diffusion model is three-dimensional with an irregular domain structure. In the future, it will be useful to predict other transport properties (permeability, fiber diffusion coefficient, conductivity, etc.) by the same technique. Another likely extension to this model is to model the transient diffusion into and swelling of the fiber wall during moisturization.

3. References

1. A. Ahmed and A. N. Alexandrou, Compression Molding using a Generalized Eulerian-Lagrangian Formulation with Automatic Remeshing, Adv. Polym. Technol. 11 (1992) 203-211.

2. M. F. Beatty, Topics in Finite Elasticity: Hyperelasticity of Rubber, Elastomers, and biological Tissues-with examples, Appl. Mech. Rev. 40 (1987) 1699-1734.

3. D. F. Benjamin, L. E. Scriven and Colleagues, Coating Flows: Form and Function, Industrial Coating Research 1 (1991) 1-37.

4. D. F. Benjamin, L. E. Scriven and Colleagues, Coaters Analyzed by Form and Function, Industrial Coating Research 2 (1992) 1-21.

5. J. C. Berg, Wettability (M. Dekker, New York, 1993).

6. R. A. Cairncross, P. R. Schunk, T. A. Baer, R. R. Rao and P. A. Sackinger, A Finite Element Method for Free Surface Flows of Incompressible Fluids in Three Dimensions. Part 1.Boundary Fitted Mesh Motion, Int. J. Numer. Methods Fluids. 33 (2000) 375-403.

7. T. A. Baer, R. A. Cairncross, P. R. Schunk, R. R. Rao and P. A. Sackinger, A Finite Element Method for Free Surface Flows of Incompressible Fluids in Three Dimensions. Part 2.Dynamic Wetting Lines, Int. J. Numer. Methods Fluids. 33 (2000) 405-427.

8. M. S. Carvalho, Roll Coating Flows in Rigid and Deformable Gaps, Ph.D. Thesis, University of Minnesota, 1996.

9. K. S. Chen, P. R. Schunk and P. A. Sackinger, Finite Element Analysis of Blade and Slot coating Flows using a Newton-Raphson Pseudo Solid Domain Mapping Technique and Unstructured Grids, Coating Fundamentals Symposium Proceedings, TAPPI Press, Atlanta, (1995) 131-152.

10. K. N. Christodoulou and L. E. Scriven, The Fluid mechanics of Slide Coating, J. Fluid Mech. 208 (1989) 321-354.

11. D. Cohen, Two-Layer Slot Coating: Flow Visualization and Modeling, M.S. Thesis, University of Minnesota, 1993.

12. E. B. Dussan V, On the Spreading of Liquids on Solid Surfaces: Static and Dynamic Contact lines, Ann. Rev. Fluid Mech. 11 (1979) 371-400.

13. I. D. Gates, Slot Coating Flows: Feasibility, Quality, Ph.D. Thesis, University of Minnesota, 1999.

14. P. M. Gresho and R. L. Lee, Don't Suppress the Wiggles- They're telling you Something, Comput. & Fluids. 9 (1981) 37-61.

15. R. Hanumanthu, Patterned Roll Coating, Ph.D.Thesis, University of Minnesota, 1996.

16. B. G. Higgins and L. E. Scriven, Capillary Pressure and Viscous Pressure Drop Set Bounds on Coating Bead Operability, Chem. Eng. Sci. 35 (1980) 673-682.

17. L. M. Hocking, A Moving Fluid Interface. Part2. The Removal of the Force Singularity by a Slip Flow, J. Fluid Mech. 79 (1977) 209-229.

18. C. Huh and L. E. Scriven, Hydrodynamic Model of Steady Movement of a Solid/ Liquid / Fluid Contact line, J. Colloid Interface Sci. 35 (1971) 85-101.

19. S. F. Kistler and P. M. Schweizer, Liquid Film Coating (Chapman and Hall, London, 1997).

20. S. F. Kistler, The Fluid Mechanics of Curtain Coating and other related Viscous Free Surface Flows with Contact Lines, Ph.D. Thesis, University of Minnesota, 1984.

21. K. S. Kundert and A. S. Vincentelli, A sparse linear equation solver, Version 1.3a, University of California, Berkeley, 1988.

22. G. R. Lester, Contact lines of liquids at deformable solid surfaces, J. Colloid Sci. 16 (1961) 315-326.

23. J. Lowndes, The Numerical Simulation of the Steady Movement of a Fluid Meniscus in a Capillary Tube, J. Fluid Mech. 101 (1980) 631-646.

24. S. Madasu and R. A. Cairncross, Static Wetting on Flexible Substrates: A Finite Element Formulation, submitted to J. Comput. Phys. (2002)

25. K. Miyamoto, On the Mechanism of Air Entrainment, Industrial Coating Research 1 (1991) 71-88.

26. J. T. Oden and G. F. Carey, Finite Elements, Mathematical Aspects, vol. IV, (Prentice Hall, New Jersey, 1983).

27. J. T. Oden and T. L. Lin, On the General Rolling Contact Problem for Finite Deformations of a Viscoelastic Cylinder, Comput. Methods Appl. Mech. Eng. 57 (1986) 297-367.

28. B. Ramaswamy, Numerical Simulation of Unsteady Viscous Free Surface flow, J. Comput. Phys. 90 (1990) 396-430.

29. P. A. Sackinger, P. R. Schunk and R. R. Rao, A Newton-Raphson Pseudo-Solid Domain Mapping Technique for Free and Moving Boundary Problems: A Finite Element Implementation, J. Comput. Phys. 125 (1996) 83-103.

30. H. Saito and L. E. Scriven, Study of Coating Flow by the Finite Element Method. J. Comput. Phys. 42 (1981) 53-76.

31. L. Sartor, Slot Coating: Fluid Mechanics and Die and Design, Ph.D. Thesis, University of Minnesota, 1990.

32. P. R. Schunk, Surfactant Polymer Effects in Coating and Related Flows, Ph.D. Thesis, University of Minnesota, 1989.

33. P. R. Schunk and R. R. Rao, Finite Element Analysis of Multicomponent Two-Phase Flows with Interphase Mass and Momentum Transport, Int. J. Numer. Methods Fluids. 18 (1994) 821-842.

34. W. J. Silliman and L. E. Scriven, Separating Flow near a Static Contact Line: Slip at a Wall and Shape of a Free Surface, J. Comput. Phys. 34 (1980) 287-313.

35. A. Soulaimani, M. Fortin, G. Dhatt and Y. Ouellet, Finite Element Simulation of

Two- and Three-Dimensional Free Surface Flows, Comput. Methods Appl. Mech. Eng. 86 (1991) 265-296.

36. J. N. Tilton, The Steady Movement of an Interface between two Viscous Liquids in a Capillary Tube, Chem. Eng. Sci. 43 (1988) 1371-1384.

37. S. Timoshenko and J. N. Goodier, Theory of Elasticity, (McGraw-Hill Book Company, New York, 1951).

38. H. P. Wang and R. T. MccLay, Automatic Remeshing Scheme for Modeling Hot Forming Process, J. Fluids Eng. 106 (1986) 465-469.

39. M. Y. Zhou and P. Sheng, Dynamics of Immiscible-Fluid Displacement in a Capillary Tube, Phys. Rev. Lett. 64 (1990) 882-885.

4. Distribution:

1	MS0834	Justine Johannes	9114
1	MS0834	Randy Schunk	9114
1	MS0834	Tom Baer	9114
1	MS0323	Yolanda Moreno	1010
1	MS9018	Central Technical File	8945-1
2	MS0899	Technical Library	9616